

The Melting of Carbonated Pelites from 70 to 700 km Depth

DANIELE GRASSI* AND MAX W. SCHMIDT

INSTITUTE OF GEOCHEMISTRY AND PETROLOGY, DEPARTMENT OF EARTH SCIENCES, D-ERDW, CLAUDIUSSTRASSE 25, CH-8092 ZURICH, SWITZERLAND

RECEIVED JUNE 17, 2010; ACCEPTED JANUARY 7, 2011
ADVANCE ACCESS PUBLICATION FEBRUARY 27, 2011

Phase assemblages, melting relations and melt compositions of a dry carbonated pelite (DG2) and a carbonated pelite with 1.1 wt % H₂O (AM) have been experimentally investigated at 5.5–23.5 GPa and 1070–1550°C. The subsolidus mineralogies to 16 GPa contain garnet, clinopyroxene, coesite or stishovite, kyanite or corundum, phengite or potassium feldspar (≤ 8 GPa with and without H₂O, respectively), and then K-hollandite, a Ti phase and ferroan dolomite/Mg-calcite or aragonite + ferroan magnesite at higher pressures. The breakdown of clinopyroxene at >16 GPa causes Na-rich Ca-carbonate containing up to 11 wt % Na₂O to replace aragonite and leads to the formation of an Na-rich CO₂ fluid. Further pressure increase leads to typical Transition Zone minerals such as the CAS phase and one or two perovskites, which completely substitute garnet at the highest investigated pressure (23.5 GPa). Melting at 5.5–23.5 GPa yields alkali-rich magnesio-dolomitic (DG2) to ferro-dolomitic (AM) carbonate melts at temperatures 200–350°C below the mantle geotherm, lower than for any other studied natural composition. Melting reactions are controlled by carbonates and alkali-hosting phases: to 16 GPa clinopyroxene remains residual, Na is compatible and the magnesio- to ferro-dolomitic carbonate melts have extremely high K₂O/Na₂O ratios. K₂O/Na₂O weight ratios decrease from 26–41 at 8 GPa to 1.2 at 16 GPa when K-hollandite expands its stability field with increasing pressure. At >16 GPa, Na is repartitioned between several phases, and again becomes incompatible as at <3 GPa, leading to Na-rich carbonate melts with K₂O/Na₂O ratios $\ll 1$. This leaves the pressure interval of c. 4–15 GPa for ultrapotassic metasomatism. Comparison of the solidus with typical subducting slab-surface temperatures yields two distinct depths of probable carbonated pelite melting: at 6–9 GPa where the solidus has a negative Clapeyron slope between the intersection of the silicate and carbonate melting reactions at ~ 5 GPa, and the phengite or potassium feldspar stability limit at ~ 9 GPa.

The second opportunity is related to possible slab deflection along the 660 km discontinuity, leading to thermal relaxation and partial melting of the fertile carbonated pelites, thus recycling sedimentary CO₂, alkalis and other lithophile and strongly incompatible elements back into the mantle.

KEY WORDS: carbonated pelites; subduction; alkali-carbonate melts; mantle metasomatism; element recycling; EM 2

INTRODUCTION

There is consensus that at sub-arc mantle depths above subducting oceanic lithosphere H₂O is the volatile component controlling fluid- and melt-producing reactions (Schmidt & Poli, 1998; Hacker *et al.*, 2003; Hacker, 2008). This is because high-pressure, low-temperature fluids have low X_{CO_2} (Connolly, 2005) and fluid-saturated minimum melting reactions at these depths result in hydrous silicate melts of pelites, basalts, and peridotites (Nichols *et al.*, 1994; Niida & Green, 1999; Schmidt *et al.*, 2004). Minimum melting of carbonated pelites yields silicate melts up to 5 GPa (Thomsen & Schmidt, 2008). However, once oceanic lithosphere subducts beyond typical sub-arc depths (i.e. >4 –7 GPa), the situation changes profoundly. Most of the H₂O has by then been expelled from the subducting lithosphere, whereas only a small fraction of the subducted carbonate decomposes below the arc (Kerrick & Connolly, 2001). Most of the CO₂ bound in subducted carbonate minerals is transported to deeper regions (Connolly, 2005) and thus is available for melting reactions at greater depth. At pressures of 8–13 GPa, carbonated

*Corresponding author. E-mail: daniele.grassi@alumni.ethz.ch

pelites melt some 200–350°C below the mantle geotherm (Grassi & Schmidt, 2011). They have the lowest melting temperature of all lithologies in the subducting lithosphere, and yield potassic magnesio- to ferro-dolomitic carbonate melts over a temperature interval from the solidus to well above the adiabat, both for H₂O-bearing and dry compositions (Grassi & Schmidt, 2011). One can thus expect that carbonate melts are produced from carbonated pelagic or psammitic sediments at the latest when subduction slows down or stops, or when the subducted lithosphere deflects along the 660 km discontinuity, continuing laterally and leaving time for thermal equilibration with the surrounding mantle. This contrasts with the melting of K-free carbonated basalts or peridotites, which have much higher melting temperatures (Dasgupta *et al.*, 2004; Yaxley & Brey, 2004; Dasgupta & Hirschmann, 2006) and would melt only upon upwelling at ≤200 km depth when adiabatic mantle temperatures exceed the conductive geotherm (Dasgupta & Hirschmann, 2006).

Of all the major lithologies subducted into the mantle, carbonated metasediments are the most fertile because of their distinct major element (K₂O, CO₂), trace element and isotopic composition (e.g. Ba, Sr, Th, Pb and Nd). In this study we aim to understand the mineralogy and reactions that govern melting, and the composition of the minimum melts derived from sediments for depths ranging from the top of the slab in the sub-arc region to just beyond the 660 km discontinuity.

EXPERIMENTAL PROCEDURES AND ANALYTICAL TECHNIQUES

Starting materials

The hydrous bulk composition with 1.1 wt % H₂O (AM, Table 1) is the same as that used by Thomsen & Schmidt (2008) and corresponds to a simplified Fe-rich calcareous clay in the system K₂O–Na₂O–CaO–FeO–MgO–Al₂O₃–SiO₂–H₂O–CO₂ (KNCFMASH–CO₂). The dry composition DG2 (Table 1) is a synthetic carbonated pelite in the TiKNCFMASH–CO₂ system (Grassi & Schmidt, 2011). Both compositions are saturated in coesite/stishovite and kyanite/corundum, and in the subsolidus with carbonates.

The starting materials were made of powders of SiO₂, Al₂O₃, TiO₂, MgO, Na₂SiO₃, and synthetic fayalite, potassium feldspar and wollastonite, milled and ground to <5 µm and then mixed with Al(OH)₃, CaCO₃ and MgCO₃ (pure natural magnesite from Obersdorf; Philipp, 1998) to introduce the desired amount of H₂O and CO₂. The powders were kept in a desiccator under ambient temperature (AM) or in a vacuum oven at 110°C (DG2).

In the following discussion, compositions are referred to in terms of their Ca:Fe:Mg ratio, which we denote as the molar ratio $X^*_{M2+} = M^{2+}/(Ca + Mg + Fe^{2+})$. To avoid

confusion, we use Mg-number = 100Mg/(Mg + Fe²⁺), also on a molar basis, to describe Mg–Fe²⁺ variations.

Experimental procedure

Experiments up to 16 GPa were conducted in a 600 ton Walker-type rocking multi-anvil. The whole multi-anvil apparatus was rotated by 180° during the experiments to improve attainment of equilibrium and to reduce chemical zonation in the capsules (Schmidt & Ulmer, 2004). The experiments were rotated continuously during the first 30 min and then every 10 min during the remainder of the experiment. At higher pressures (18–23.5 GPa), a conventional 1000 ton Walker-type multi-anvil was used.

Tungsten carbide cubes with truncation edge lengths of 11 mm (5.5–8 GPa), 8 mm (13 GPa) and 3.5 mm (16–23.5 GPa) were combined with prefabricated MgO octahedra of 18, 14, and 10 mm edge length, respectively, and with natural pyrophyllite gaskets. Assemblies consisted of a zirconia insulator, a stepped LaCrO₃ furnace (straight for the 10/3.5 assembly), inner MgO parts and Mo end disks and rings. Details of the experiments at 8 and 13 GPa have been described by Grassi & Schmidt (2011) and for the smaller 10/3.5 assembly by Stewart *et al.* (2006).

Temperature was controlled using a B-type (Pt₉₄Rh₆/Pt₇₀Rh₃₀) thermocouple; no correction for the effect of pressure was applied. Two Au₈₀Pd₂₀ capsules were used in each experiment, stacked in the central part of the furnace assembly just below the thermocouple. Typical thermal gradients across a capsule are 10–20°C. Quenching was done by turning off the heating power and was followed by pressure unloading over about 15–20 h.

The starting material contained fayalite as the only iron source, hence all Fe is assumed to be Fe²⁺ at the beginning of each experiment. All carbon was added as carbonate and the absence of graphite/diamond in the experiments suggests an oxygen fugacity at least slightly above the graphite/diamond–CO–CO₂ (CCO) buffer. On the other hand, the absence of graphite/diamond also indicates that no major redox reaction between Fe and C has taken place. Some minor oxidation might occur through diffusive hydrogen loss in the AM composition, but normalized garnet and cpx compositions do not indicate any significant Fe³⁺ component. We thus assume that oxygen fugacity in the experiments was slightly above the CCO buffer but did not reach the quartz–fayalite–magnetite (QFM) buffer. This oxygen fugacity range is expected to correspond to that of subducting crust in which carbon is maintained in its oxidized form.

Capsules were mounted longitudinally in epoxy resin and polished to the centre using a dry polishing method to avoid loss of alkalis from the alkali-rich carbonates and quenched carbonate melts. Additionally, the open capsules were repeatedly embedded in low-viscosity resin to avoid chemical and mechanical loss of quench carbonate melts.

Table 1: Bulk starting compositions and near-solidus melt compositions

Run no.:	AM*	AM-19*	AM-07*	ME-110*	AM-24*	ME-110*	am-32†	am-5B	am-9	am-25	am-19	S6a‡
<i>P</i> (GPa):		2.5	3.7	5	3.7	5	5.5	8	13	16	18	22
<i>T</i> (°C):		900	1000	1100	1100	1100	1180	1000	1200	1350	1400	1500
No. analyses:		7	6	4	12	7	8	11	13	6	5	21
SiO ₂ (wt %)	47.60	66.9 (1.7)	64.9 (1.1)	59.2 (1.3)	0.91 (0.7)	0.62 (0.4)	2.44 (1.4)	0.30 (0.1)	0.48 (0.2)	0.61 (0.5)	0.3 (0.2)	0.04 (0.1)
TiO ₂	-	-	-	-	-	-	-	-	-	-	-	-
Al ₂ O ₃	22.80	19.0 (1.2)	20.3 (1.0)	18.4 (1.5)	0.97 (0.5)	0.87 (0.3)	2.35 (0.5)	1.85 (0.3)	1.35 (0.2)	0.95 (0.2)	1.2 (0.4)	0.30 (0.1)
FeO	9.20	0.72 (0.4)	1.09 (0.1)	3.06 (0.8)	8.76 (0.8)	11.9 (0.7)	10.5 (1.1)	12.1 (0.9)	9.50 (0.8)	9.50 (0.4)	10.5 (1.5)	9.35 (0.2)
MgO	2.00	0.07 (0.3)	0.13 (0.1)	0.50 (0.2)	3.62 (0.3)	3.76 (0.4)	2.63 (0.9)	2.10 (0.2)	2.32 (0.3)	3.51 (0.5)	4.5 (0.8)	6.02 (0.3)
CaO	6.80	0.70 (0.9)	0.46 (0.1)	2.45 (0.5)	30.8 (2.1)	30.1 (1.7)	28.9 (6.9)	16.5 (0.8)	25.5 (1.4)	25.5 (2.2)	26 (2.3)	20.1 (0.2)
Na ₂ O	2.40	1.71 (0.6)	1.37 (0.2)	2.44 (0.2)	4.01 (2.1)	1.97 (0.6)	2.33 (0.4)	0.65 (0.2)	4.8 (0.6)	7.7 (1.5)	10.5 (3.1)	19.6 (0.3)
K ₂ O	3.60	10.9 (1.1)	11.7 (0.9)	14.0 (0.8)	0.71 (0.2)	4.21 (0.7)	8.33 (4.3)	26.8 (1.7)	10.2 (1.7)	8.7 (1.3)	4.5 (0.9)	3.37 (0.2)
H ₂ O [§]	1.10	3.4	3.2	3.7	n.a.	n.a.	n.a.	9.4	9.88	n.a.	9.5	n.a.
CO ₂ [§]	4.80	2.4	2.2	2.2	48.9 (2.4)	47.6 (4.4)	n.a.	38.5	43.1	n.a.	37.0	n.a.
Total	100.30	91.80	90.10	87.10	49.78	53.43	57.50	60.35	54.13	56.47	57.50	58.73
Si (a.p.f.u.)¶		3.02	2.95	2.81	0.03	0.02	0.24	0.01	0.02	0.06	0.01	0.00
Ti		-	-	-	-	-	-	-	-	-	-	-
Al _{tot}		1.01	1.09	1.03	0.04	0.03	0.28	0.06	0.05	0.12	0.04	0.01
Fe _{tot}		0.03	0.04	0.12	0.26	0.34	0.87	0.29	0.25	0.84	0.25	0.19
Mg		0.01	0.01	0.04	0.19	0.19	0.39	0.09	0.11	0.56	0.19	0.22
Ca		0.03	0.02	0.13	1.17	1.10	3.08	0.51	0.87	2.91	0.78	0.53
Na		0.15	0.12	0.23	0.28	0.13	0.45	0.04	0.30	1.59	0.57	0.94
K		0.63	0.68	0.85	0.03	0.18	1.06	0.99	0.41	1.18	0.16	0.11
K ₂ O/Na ₂ O (wt %)	1.50	6.39	8.59	5.73	0.18	2.24	3.57	41.31	2.13	1.13	0.43	0.17
<i>D</i> _{Na} ^{cp/melt} (wt %)	-	3.10	7.32	3.58	2.20	5.43	3.70	16.06	2.71	1.67	-	-
Mg-no.	27.90	25.00	20.00	25.00	42.22	35.85	30.90	23.68	30.56	39.71	43.18	53.66
X _{Mg} (Fetot) (molar)	0.17	0.14	0.14	0.14	0.12	0.12	0.09	0.10	0.09	0.14	0.15	0.23
X _{Ca} (molar)	0.41	0.43	0.29	0.45	0.72	0.67	0.71	0.57	0.71	0.71	0.64	0.56
Run no.:	DG2	DG2-32†	DG2-3	reverse	DG2-27	DG2-19‡	S5a	DG2-15				
<i>P</i> (GPa)/ <i>T</i> (°C):		5.5/1180	8/1100	13/1350	16/1350	18/1400	22/1500	22/1550				
No. analyses:		8	13	14	7	12	19	14				
SiO ₂ (wt %)	54.63	3.24 (3.1)	0.26 (0.1)	0.22 (0.1)	0.99 (0.5)	0.09 (0.1)	0.05 (0.1)	0.07 (0.1)				
TiO ₂	0.63	2.47 (0.6)	2.37 (0.4)	1.83 (0.3)	1.70 (0.2)	1.03 (0.8)	0.56 (0.1)	0.47 (0.1)				
Al ₂ O ₃	20.23	2.58 (1.2)	1.55 (0.3)	1.18 (0.3)	1.15 (0.4)	0.82 (0.3)	0.26 (0.1)	0.44 (0.1)				
FeO	4.86	8.87 (2.1)	7.55 (0.6)	7.08 (0.6)	6.91 (1.2)	5.17 (1.1)	7.32 (0.2)	4.36 (0.4)				
MgO	2.92	6.46 (0.7)	2.95 (0.3)	5.35 (0.3)	5.92 (0.8)	4.67 (0.7)	7.36 (0.6)	11.1 (1.1)				
CaO	5.88	21.7 (4.3)	16.3 (1.5)	26.4 (1.2)	25.1 (1.7)	19.8 (4.1)	15.3 (0.2)	15.9 (2.1)				
Na ₂ O	3.20	1.71 (0.3)	0.95 (0.6)	4.71 (0.6)	7.02 (1.1)	17.5 (5.1)	22.7 (0.8)	20.1 (1.1)				
K ₂ O	2.21	7.31 (2.1)	24.4 (2.8)	9.43 (1.1)	8.79 (1.9)	4.03 (1.1)	3.27 (0.2)	4.97 (0.5)				
H ₂ O [§]	-	-	-	-	-	-	-	-				
CO ₂ [§]	4.50	45.70	43.67	43.80	42.42	46.78	43.12	42.64				
Total	99.07	100.00	100.00	100.00	100.00	100.00	100.00	100.00				
Si (a.p.f.u.)¶		0.32	0.01	0.01	0.10	0.00	0.00	0.00				
Ti		0.18	0.05	0.04	0.13	0.02	0.01	0.01				
Al _{tot}		0.30	0.06	0.04	0.13	0.03	0.01	0.01				
Fe _{tot}		0.73	0.19	0.18	0.57	0.12	0.15	0.09				
Mg		0.94	0.14	0.24	0.88	0.19	0.27	0.40				
Ca		2.27	0.54	0.85	2.67	0.58	0.40	0.41				
Na		0.33	0.06	0.28	1.35	0.93	1.07	0.93				
K		0.91	0.96	0.36	1.11	0.14	0.10	0.15				
K ₂ O/Na ₂ O (wt %)	0.69	4.27	25.68	2.00	1.25	0.23	0.14	0.25				
<i>D</i> _{Na} ^{cp/melt} (wt %)	-	5.55	10.00	2.37	1.76	-	-	-				
Mg-no.	52.10	56.50	42.42	57.14	60.69	61.29	64.29	81.63				
X _{Mg} (Fetot) (molar)	0.30	0.24	0.16	0.19	0.21	0.21	0.33	0.44				
X _{Ca} (molar)	0.43	0.58	0.62	0.67	0.65	0.65	0.49	0.46				

*Thomsen & Schmidt (2008).

†Average of various strong heterogeneous single analyses (no reverse available and no mass-balance correction).

‡Reversed.

§H₂O and CO₂ content calculated from bulk and melt fraction (if no H₂O present CO₂ content calculated by difference of 100 and the measured analytical total).

¶Cations calculated on the basis of six oxygens for carbonates and eight oxygens for silicate melts.

After analysis the capsules were stored in a desiccator under vacuum.

Analytical methods and iterative sandwich experiments

All experimental charges were analyzed with a JEOL JXA8200 electron microprobe at ETH-Zürich employing 15 kV acceleration voltage, 20 nA beam current for silicate minerals and 5 nA for carbonates and carbonate melts. Acquisition times were 10 s for Na and K and 20 s for all other elements, measuring Na and K first to avoid diffusional losses. Beam diameters of 1–2 μm were used for silicates and carbonates. Quenched melts, which are susceptible to beam damage, were analyzed, whenever possible, using a defocused beam (3–20 μm). Because of the uncertainty in the analysis of small pools of quenched carbonate melt, we have reversed melt compositions at the solidus using an iterative sandwich technique in which about 50% melt is loaded between two layers of the original bulk composition [for a detailed description see Grassi & Schmidt (2011)]. In these sandwich experiments the composition of the melt layer is adjusted iteratively such that the same phases with the same compositions are present in both the forward and the final sandwich melting experiment. The resultant large melt pools (>200 μm) allow us to verify melt compositions without the analytical difficulties inherent in small alkaline-rich carbonate melt pools. We have thus verified the composition of the near-solidus melts and the conditions of melting by 1–5 iterations at 8, 13, 16 and 22 GPa. Only at 5.5 and 18 GPa were the melt pools at the solidus sufficiently large (>40 μm) to be directly measured with confidence.

Secondary and back-scattered electron images from the microprobe or from a JEOL JSM6300 field emission scanning electron microscope were used for textural analysis. Micro-Raman spectroscopy was employed to identify carbonate polymorphs, potassium feldspar/K-hollandite and Ti-oxides at 8 GPa, perovskite at $P > 18$ GPa, and to identify the structure of the Na-carbonate, which is similar to that of calcite and dolomite.

RESULTS

In total, 38 experiments were performed on the 1.1 wt % H_2O AM composition (Fig. 1; this study; 8 and 13 GPa: Grassi & Schmidt, 2011; ≤ 5 GPa: Thomsen & Schmidt, 2008) and 24 experiments on the dry DG2 composition (this study; 8 and 13 GPa: Grassi & Schmidt, 2011). Mineral proportions and run conditions for the experiments of this study are presented in Table 2; subsolidus mineral proportions calculated using least-squares regression analysis are plotted in Fig. 2 as a function of pressure. Equilibrium in the experiments is indicated by the presence of well-crystallized grains, 120° triple point junctions between phases (Fig. 3) and a homogeneous composition of the various minerals throughout the capsule. Mineral

compositional trends as a function of pressure and temperature also suggest that equilibrium was generally reached. This result was achieved only after prolonging run times from 24 to 96 h. Runs of 24 h duration were in textural disequilibrium, and at sub- and near-solidus conditions, the minerals were too small to be reliably analysed by electron microprobe. Nevertheless, despite run times of 96 h at 1400°C (e.g. run 29 at 23.5 GPa), some phases remained small ($< 5 \mu\text{m}$) at subsolidus conditions, making them difficult to analyse.

Subsolidus phase assemblages

Subsolidus assemblages change with increasing pressure (Figs 1 and 2), and consist of garnet, quartz/coesite, kyanite, clinopyroxene, phengite (in the H_2O -bearing AM bulk) or potassium feldspar (in the dry DG bulk) and Mg-rich calcite (AM) or ferroan dolomite (DG2) at 2.5–6.5 GPa (Fig. 2). When pressure is increased from 6.5 to 8 GPa, Mg-calcite or ferroan dolomite are replaced by ferroan magnesite + aragonite, which coexist in both compositions up to 16 GPa. At 8 GPa the stable K phases are phengite or potassium feldspar, which are both replaced by K-hollandite at higher pressures (*c.* 9 GPa, Schmidt *et al.*, 2004; Yong *et al.*, 2006). After the breakdown of phengite, no other hydrous phases could be detected in the AM composition; thus, the presence of an H_2O -rich fluid is likely in the AM experiments at $P > 9$ GPa. At 12.5 GPa (1000°C), kyanite dissociates to stishovite and corundum (Schmidt *et al.*, 1997). Clinopyroxene is stable to 16 GPa; its breakdown causes Na-rich Ca-carbonate with up to 11 wt % Na_2O to replace aragonite. At 18 GPa, the subsolidus assemblage consists of stishovite, corundum, garnet, K-hollandite, ferroan magnesite and Na-rich Ca-carbonate. This assemblage changes at 22 GPa, where characteristic high-pressure phases such as Ca-perovskite, FeTi-perovskite, and the CAS phase ($\text{CaAl}_4\text{Si}_2\text{O}_{11}$, Gautron *et al.*, 1997; Table 3), the last only above the solidus at $T \geq 1400^\circ\text{C}$, progressively substitute for garnet. In the DG2 composition at 8 and 13 GPa, small amounts of rutile II (TiO_2 with $\alpha\text{-PbO}_2$ structure; Simons & Dacheille, 1967) crystallize at subsolidus conditions. In the hydrous AM composition, minute grains of an almost pure Fe-oxide are observed at 22 GPa. Throughout the investigated P – T conditions, all experiments are SiO_2 - as well as Al_2O_3 -saturated.

Mineral compositions and stability

Garnet (Grt) forms homogeneous, mostly inclusion-free subidiomorphic 5–30 μm size crystals (Fig. 3). With increasing pressure the Mg-number of garnets generally increases from 16.9 to 29.7 for AM and from 22.7 to 40.0 for DG2 (Fig. 4). Nevertheless, discrete decreases in the Mg-number of garnets are observed in both compositions at 5.5–8 GPa when ferroan magnesite + aragonite replace Mg-calcite or ferroan dolomite, and in the AM

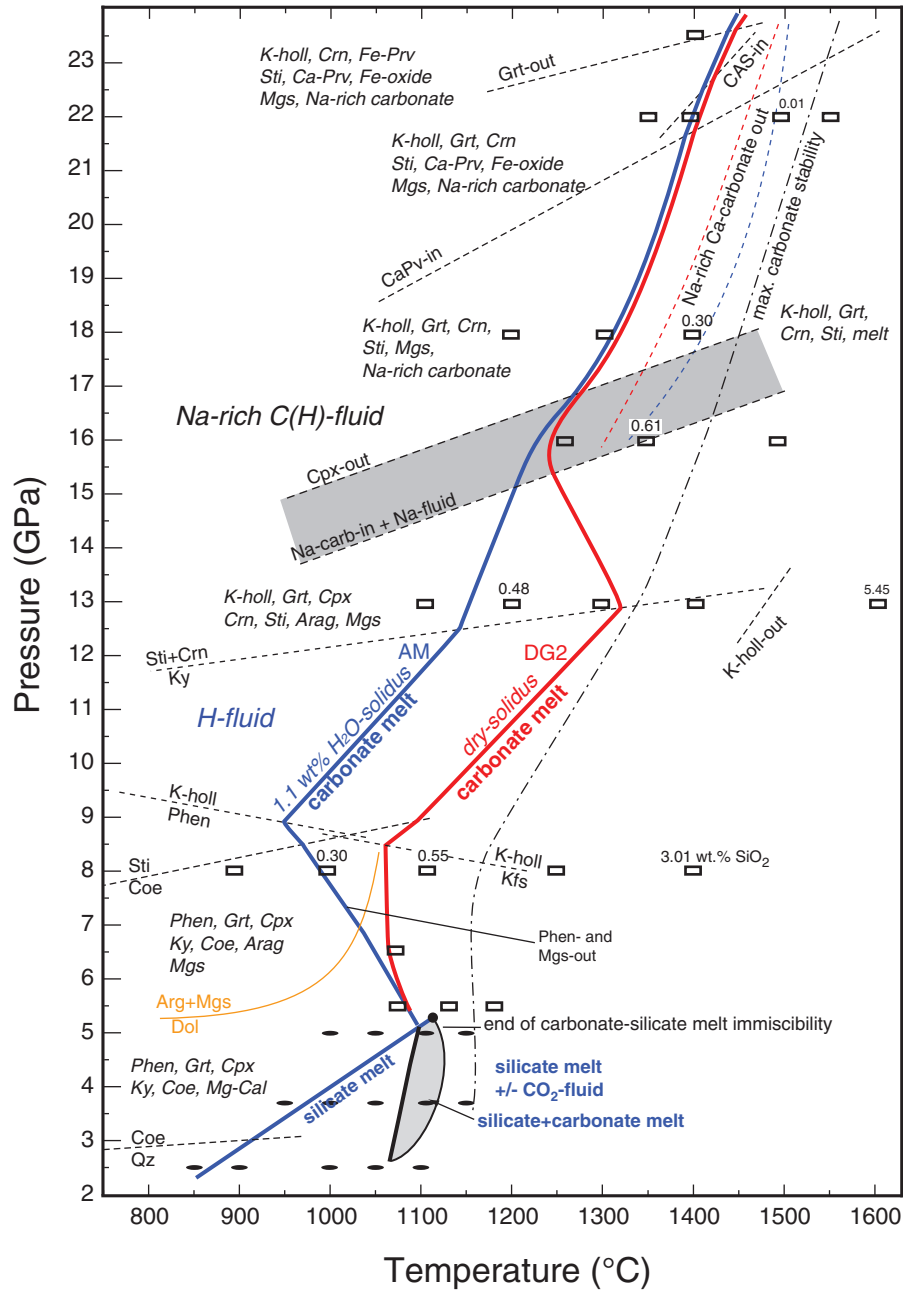


Fig. 1. P - T diagram compiled from experimental studies of carbonated pelites from 2.5 to 23.5 GPa in the system TiKNCFMASH- CO_2 . The bold blue line represents the solidus of the 1.1 wt % H_2O , Ti-free AM composition, whereas the bold red line represents the solidus of the dry DG2 composition. Small black ellipses are experiments on AM by Thomsen & Schmidt (2008). All rectangles represent experiments on both compositions; at 8 and 13 GPa these are from Grassi & Schmidt (2011), at 5.5–6.5 and 16–23.5 GPa from this study. The solidus at >9 GPa for the AM and at >16 GPa for DG2 represents a fluid-present solidus; at lower pressures the solidi are fluid-absent. Numbers above experimental symbols refer to SiO_2 contents (wt %) in the melts for AM. Changes in the slope of the solidi are drawn according to Schreinemaker rules at the intersections with coesite = stishovite (Zhang *et al.*, 1996), the decomposition reaction of kyanite to corundum + stishovite (Schmidt *et al.*, 1997; this study), the phengite to K-hollandite reaction (Schmidt *et al.*, 2004), the Kfs to K-hollandite reaction, the cpx- and garnet-out reactions (this study), and the Ca-perovskite- and CAS-in reactions (this study). It should be noted that the slope and exact location of the Kfs to K-hollandite reaction is unknown. Above 8 GPa, the temperature stability of K-hollandite is strongly bulk composition dependent. At 13 GPa the 1.1 wt % AM composition with the higher K_2O content has K-hollandite coexisting with the melt to 1400°C (i.e. 200°C above the solidus); the dry DG2 composition has no K-hollandite above 1350°C. The dolomite to aragonite + magnesite reaction is from Buob *et al.* (2006). Arag, aragonite; CAS, $\text{CaAl}_4\text{Si}_2\text{O}_{15}$; Coe, coesite; Cpx, clinopyroxene; Crn, corundum; Dol, dolomite; Grt, garnet; Kfs, potassium feldspar; K-holl, potassium hollandite; Ky, kyanite; Mgs, magnesite; Mg-Cal, magnesium calcite; Na-carb, Na-rich carbonate; Phen, phengite; Prv, perovskite; Sti, stishovite.

Table 2: *Experimental run conditions and phase assemblages*

Run no. & bulk	<i>P</i> (GPa)	<i>T</i> (°C)	Time (h)	Phen	Kfs	K-holl	Arag	Mgs	Dol	Mg-Cal	Na-carb	oxide	Grt	Cpx	CAS	Ca-Prv	Fe-Prv	Ky	Crn	Coe/ Sti	Carb. melt
DG2-22	5.5	1070	96	-	13.4	-	-	-	9.9	-	-	x	10	32.8	-	-	-	16.8	-	17.1	-
DG2-31	5.5	1125	72	-	-	-	-	-	-	-	-	-	xx	xxx	-	-	-	xx	-	xx	x
DG2-32	5.5	1180	48	-	-	-	-	-	-	-	-	-	xx	xxx	-	-	-	xx	-	xx	xx
DG2-30	6.5	1070	72	-	-	-	-	-	x	-	-	-	xxx	xxx	-	-	-	xx	-	xx	x
DG2-25	16	1250	96	-	-	14.3	-	4.3	-	-	6.1	-	21.9	15.9	-	-	-	-	9.8	27.6	x
DG2-27	16	1350	72	-	-	9.9	x	2.4	-	-	-	-	22.9	19.0	-	-	-	-	9.2	27.1	6.9
DG2-24	18	1200	96	-	-	xxx	-	x	-	-	xx	-	xxx	-	-	-	-	-	xx	xx	-
DG2-26	18	1300	72	-	-	15.8	-	2.6	-	-	13.3	-	21.9	-	-	-	-	-	13.1	33.3	-
DG2-19	18	1400	48	-	-	11.1	-	2.4	-	-	-	-	27.9	-	-	-	-	-	13.0	34.9	10.8
DG2-17	22	1350	96	-	-	14.6	-	1.8	-	-	9.5	-	23.6	-	-	x	x	-	12.9	33.6	-
DG2-28	22	1400	96	-	-	xx	-	x	-	-	xx	-	xx	-	xx	x	x	-	xx	xx	x
DG2-13	22	1500	48	-	-	8.4	-	x	-	-	-	-	18.7	-	28.3	-	-	-	x	30.4	10.9
DG2-15	22	1550	48	-	-	8.9	-	-	-	-	-	-	12.6	-	28.1	-	-	-	2.7	35.9	11.7
Dg2-29	23.5	1400	96	-	-	15.5	-	2.1	-	-	10.3	-	5.2	-	-	5.2	10.3	-	15.5	36.1	-
am-22	5.5	1070	96	29.9	x	-	-	-	10.2	-	-	-	21.7	20.8	-	-	-	9.9	-	7.6	-
am-31	5.5	1125	72	-	-	-	-	-	x	-	-	-	xxx	xxx	-	-	-	xx	-	xx	xx
am-32	5.5	1180	48	-	-	-	-	-	-	-	-	-	xxx	xxx	-	-	-	xx	-	xx	xx
am-30	6.5	1070	72	-	x	-	-	-	x	-	-	-	xxx	xxx	-	-	-	xx	-	xx	x
am-25	16	1250	96	-	-	24.3	-	2.3	-	-	9.1	-	29.2	-	-	-	-	-	12.6	22.5	x
am-27	16	1350	72	-	-	20.5	x	2.3	-	-	-	-	29.8	11.4	-	-	-	-	9.6	17.9	8.5
am-24	18	1200	96	-	-	xxx	-	x	-	-	xx	-	xxx	-	-	-	-	-	xx	xx	-
am-26	18	1300	72	-	-	25.5	-	2.5	-	-	9.3	-	29.8	-	-	-	-	-	12.2	20.7	-
am-19	18	1400	48	-	-	xx	-	x	-	-	x	-	xxx	-	-	-	-	-	xx	xxx	x
am-17	22	1350	96	-	-	26.9	-	-	-	-	12.2	2.1	13.0	-	-	3.0	6.0	-	14.0	23.0	-
am-28	22	1400	96	-	-	xxx	-	x	-	-	xx	-	xx	-	xx	x	x	-	xx	xx	x
am-13	22	1500	48	-	-	22.9	-	1.5	-	-	-	-	26.1	-	11.1	-	-	-	8.6	19.6	10.8
am-15*	22	1550	48	-	-	xx	-	-	-	-	-	-	xxx	-	xxx	-	-	-	xx	xx	-
am-29	23.5	1400	96	-	-	29.9	-	-	-	-	13.0	2.0	-	-	-	5.0	11.4	-	13.8	24.9	-
DG2-S5a†	22	1500	50	-	-	xx	-	x	-	-	-	-	xx	-	xx	-	x	-	xx	xx	xxx
AM-S6a†	22	1500	50	-	-	xx	-	-	-	-	-	-	xx	-	xx	-	-	-	xx	xx	xxx

Mineral and melt modes determined by mass-balance calculations (least-squares regression analysis). Grt, garnet; Cpx, clinopyroxene; Phen, phengite; Kfs, potassium feldspar; K-holl, potassium hollandite; Sti, stishovite; Coe, coesite; Crn, corundum; Ky, kyanite; Prv, perovskite; CAS, $\text{CaAl}_4\text{Si}_2\text{O}_{11}$ (Gautron *et al.*, 1997); Dol, dolomite; Mgs, magnesite; Mg-cal, magnesium calcite; Arag, aragonite; Na-carb, Na-rich carbonate; oxide, Fe-oxide, FeTi-oxide or Ti-oxide. Subsolidus experiments include H_2O and CO_2 as mass-balance components. FeO adjusted for Fe loss to the capsule in all experiments with large amount of melt. TiO_2 was excluded during mass-balance calculation.

*Hole in the capsule (no melt or carbonates).

†Reverse experiments.

composition at 16–18 GPa when Na-rich carbonate, which contains 2–3 wt % MgO , replaces pure aragonite. Si contents in garnet remain below 3.00 Si p.f.u. to 8 GPa, then increase slightly with pressure to 3.05 p.f.u. at 13 GPa and 3.25–3.30 p.f.u. at 22–23.5 GPa in both bulk compositions (Fig. 4a). Na contents follow a similar trend and increase with pressure from near detection limit at 2.5 GPa to 0.19 Na p.f.u. (for DG2) at 23.5 GPa. Most of the Si (and Ti)

in excess, with respect to 3 Si p.f.u., charge compensate for Na in a $(\text{Ca,Fe,Mg})_{-1}\text{Al}_{-1}(\text{Na,K})(\text{Ti,Si})$ substitution. A majorite component resulting from Tschermaks substitution equal to $(\text{Si} + \text{Ti}) - 3 - (\text{Na} + \text{K})$ is significant only in the lowest temperature experiments at 18–23.5 GPa where it remains ≤ 10 mol %. These low majorite contents result from the presence of kyanite/corundum, which forces garnets to remain on the Al_2O_3 -saturation surface,

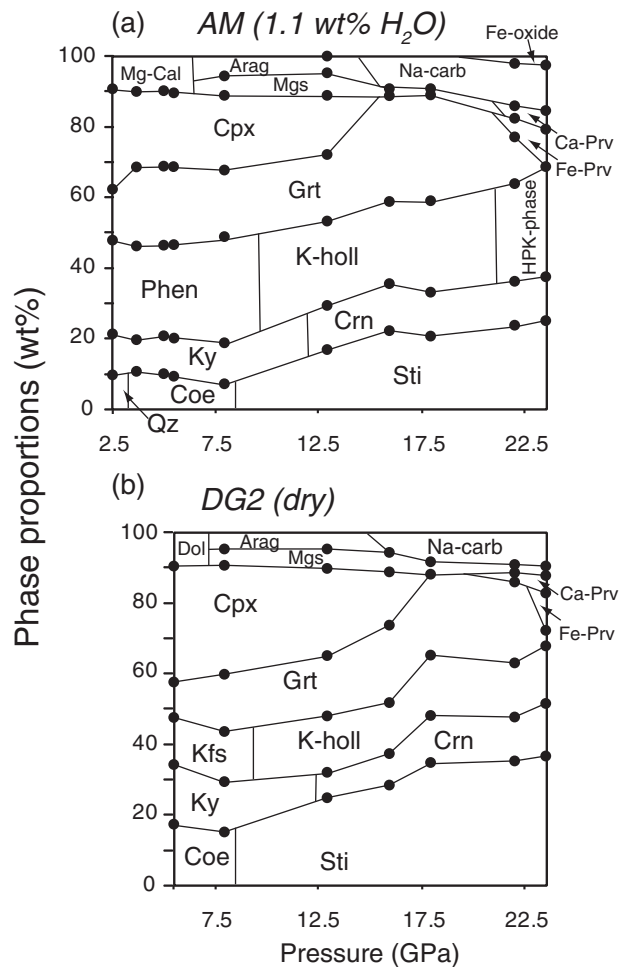


Fig. 2. Calculated modes of minerals (in wt %) at the solidus for the coesite/stishovite + kyanite/corundum-saturated, fertile carbonated metapelite AM (a) and DG2 (b) as a function of pressure. At $P > 16$ GPa some uncertainty in the mass balance is introduced by the presence of an Na-rich fluid, dissolving significant but unknown quantities of elements. The AM bulk has 1.1 wt % H_2O and crystallizes phengite at $P < 9$ GPa; DG2 is dry. Different amounts of Na_2O and K_2O in the bulk are reflected in the proportions of cpx and phengite/Kfs/K-hollandite. The lower X^*_{Mg} of the AM composition causes the appearance of Mg-calcite at low pressures, whereas ferroan dolomite is stable in the higher X^*_{Mg} DG2 composition. The increasing X^*_{Mg} of garnet and Na-carbonate with pressure leads to the disappearance of magnesite at 22 GPa in the AM composition. The highest amount of garnet is observed between 16 and 18 GPa after the cpx breakdown and before perovskite formation. Abbreviations as in Fig. 1.

the latter representing the minimum majorite component stable at a given P - T condition. The TiO_2 concentration in garnet increases with pressure to 1.44 wt % at 8 GPa, reaching a maximum of 1.91 wt % at 18 GPa. At 22 and 23.5 GPa, Ti concentrations in garnet are much lower (0.32–1.33 wt %). This is attributed to the presence of Ti-rich Ca- and Fe-perovskites, and the preferential partitioning of Ti in these phases relative to garnet (see below).

The potassium concentration in garnet increases from 0.07 to 0.21 wt % (AM composition) as pressure increases from 2.5 to 8 GPa. The K contents then decrease between 8 and 18 GPa, but increase again at 22 GPa, reaching 1.08–1.15 wt % K_2O at subsolidus conditions. These high potassium contents in garnet at $P > 22$ GPa are similar to those of Wang & Takahashi (1999) in a K-rich basaltic composition.

At 23.5 GPa garnet has disappeared from the low X^*_{Mg} AM composition but 5–10 wt % remain present in DG2, where garnet coexists with Ca- and Fe-Ti-perovskite. The transition from a garnet-bearing to a garnet-free perovskite-bearing assemblage in an Fe-rich system at 23–24 GPa has also been observed by Rapp *et al.* (2008). The presence of an H_2O -bearing fluid in the AM composition might allow for some oxidation of Fe through hydrogen loss. The low Mg-number and the high FeO content of the AM composition are most probably responsible for the earlier disappearance of garnet and the larger amount of Fe-perovskite in the AM composition. Nevertheless, a slight oxidation could contribute to a lower pressure formation of Fe-perovskite known to accommodate larger amounts of Fe^{3+} than garnet (McCammon & Ross, 2003; Litasov & Ohtani, 2005).

Clinopyroxene (cpx) is stable to ≤ 16 GPa in both compositions and forms relatively small $< 15 \mu m$ long prismatic crystals. In the AM composition clinopyroxene breaks down at 16 GPa where the clinopyroxene-bearing assemblage in equilibrium with carbonate melt (at 1350°C) is replaced by a subsolidus assemblage with a Na-rich carbonate at 1250°C. In the experiments with the anhydrous composition DG2, clinopyroxene is always present at 16 GPa. The lowest temperature experiment (1250°C) has the Na-rich Ca-carbonate in addition to cpx in the same capsule but in different zones and not in direct contact. These observations suggest that in the DG2 bulk, with its higher Na_2O content and slightly higher X^*_{Ca} , the reaction from jadeitic cpx to Na-rich carbonate takes place at slightly lower temperature/higher pressure than in the AM composition. The occurrence of cpx and Na-rich Ca-carbonate in DG2 at 16 GPa, 1250°C may be interpreted in terms of P - T conditions exactly on the cpx-out reaction boundary, but may also stem from a slight phase segregation throughout the capsule.

In cpx, jadeite ($NaAlSi_3O_8$) is the most abundant component. In the AM composition it increases from Jd_{48} at 2.5 GPa to Jd_{72} at 3.5 GPa (Thomsen & Schmidt, 2008) and to Jd_{90} at 13 GPa (Fig. 5). At 16 GPa the cpx coexisting with carbonate melt is Jd_{84} . In the DG2 composition, jadeite increases from Jd_{65} to Jd_{94} at 5.5–16 GPa (Fig. 5). The Ca-Tschermak ($CaAl_2SiO_6$) component is significant only at 2.5 GPa (11 mol %), decreases considerably from 2.5 to 3.7 GPa, and is zero at 8 GPa. The Ca-eskolaite ($\square_{0.5}Ca_{0.5}AlSi_2O_6$) component does not show any

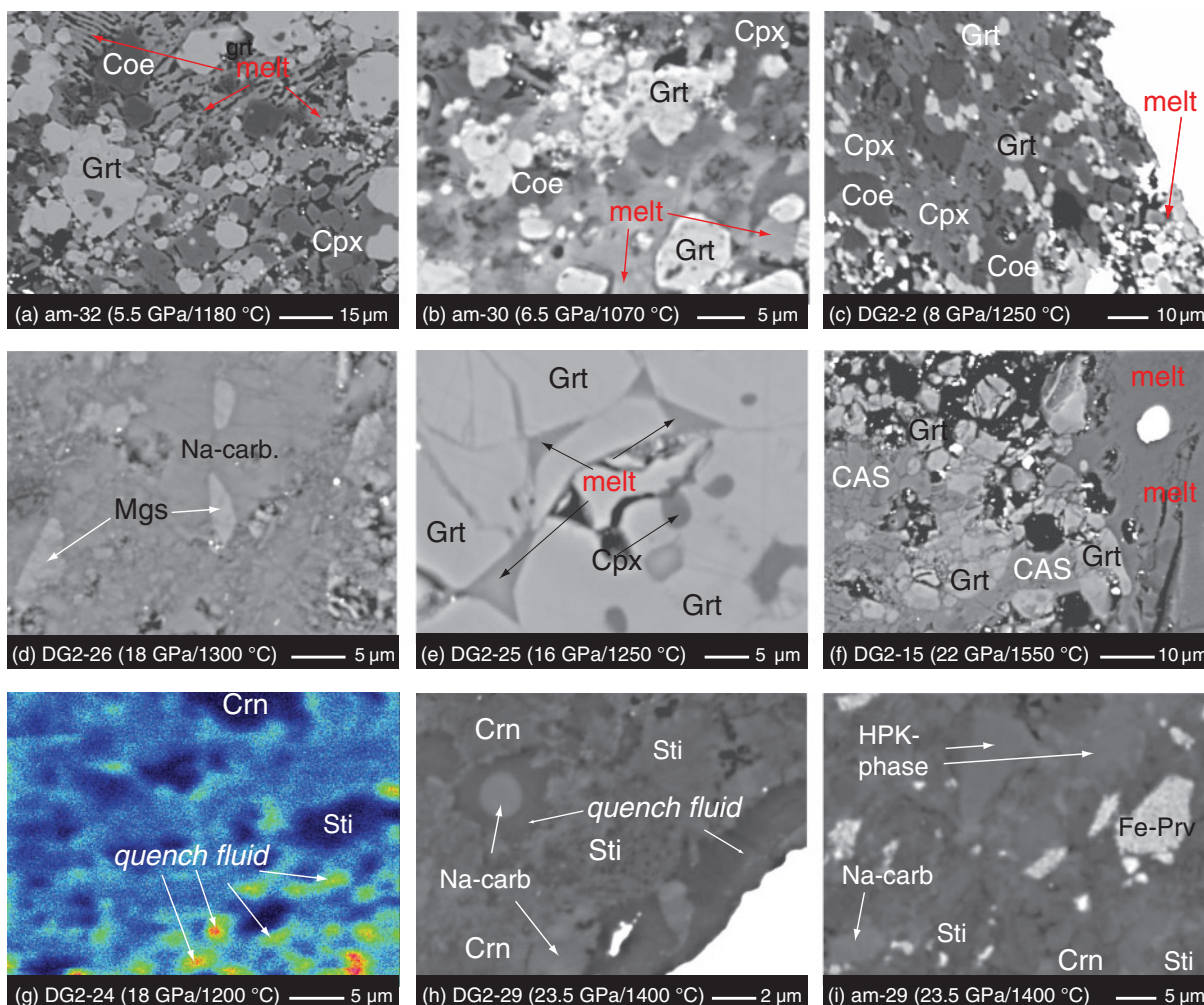


Fig. 3. Back-scattered electron (BSE) images of run products. (a) 5.5 GPa, 1180°C, bulk AM; large amounts of K-rich carbonate melt (*c.* 15 wt %) coexist with garnet, cpx, coesite and kyanite. At similar temperatures but 5 GPa, the same bulk composition yields *c.* 45 wt % of silicate melt (Thomsen & Schmidt, 2008). (b) 6.5 GPa, 1070°C, bulk AM; first small amount of potassic carbonate melt coexisting with garnet, cpx, coesite, kyanite and minor amounts of Kfs and Mg-calcite (not shown). Melt appearing homogeneous in any of the BSE images is heterogeneous and composed of quench visible only at higher magnification. (c) 8 GPa, 1250°C, bulk DG2; at 100°C above the solidus garnet, cpx, kyanite and coesite coexist with small, heterogeneous melt pockets concentrated along the margins of the capsule (lower right corner). (d) 18 GPa, 1300°C, bulk DG2; at subsolidus conditions and >16 GPa a Na-rich carbonate coexists with ferroan magnesite. The fine-grained matrix consists of the same two carbonates plus stishovite and K-hollandite. (e) 16 GPa, 1250°C, bulk DG2; first amount of melt at 16 GPa trapped at triple junctions of garnet. (f) 22 GPa, 1550°C, bulk DG2; a relatively large quantity of carbonate melt coexists with garnet and the CAS phase (and with magnesite, K-hollandite, stishovite and corundum, not shown). (g) 18 GPa, 1200°C, bulk DG2; Na-K α element distribution map of the subsolidus high-pressure assemblage. Small interstitial Na-rich patches, which do not contain Ca and which are low in Si, are interpreted as quench of a Na₂O–CO₂ fluid and are observed throughout the entire capsule. From this observation we deduce that cpx breakdown leads to a Na-rich Ca-carbonate (not visible) and a Na-rich CO₂ fluid. (h) 23.5 GPa, 1400°C, bulk DG2; two Na-rich carbonates are observed. The Na-rich carbonate with *c.* 20 wt % of Na₂O but almost no Fe and Mg (<1 mol %) is interpreted as a quench product from a fluid. (i) 23.5 GPa, 1400°C, bulk AM; near-solidus experiment crystallizing Fe-perovskite coexisting with stishovite, corundum, Na-carbonate, CAS phase, an Fe-oxide and the potassium-rich HPK phase. It should be noted that the carbonate melt compositions cannot be reliably measured in the textures shown in (a)–(c) and (e). The melt compositions in this study were measured from textures similar to those shown in (f) or from iterative sandwich experiments, which yielded large melt pools.

particular trend with pressure, although slightly increased contents are observed at intermediate pressures (9 mol % at 3.7 GPa in AM and 4 mol % at 8 GPa in DG2). In both compositions, the amount of TiO₂ and K₂O in cpx

decreases from 8 to 16 GPa (Fig. 5). A maximum amount of K₂O (0.42 wt % in AM, 1.02 wt % in DG2) is reached at 8 GPa, 900°C, similar to garnet, which also has high K contents at 8 GPa.

Table 3: Mineral compositions

Run:	am-1	am-12	DG2-1	am-29	DG2-27	DG2-28	DG2-8	DG2-17	DG2-17	DG2-24
Phase:	Phen	K-holl	Kfs	HPK phase	Cpx	Grt	CAS	Ca-Prv	Fe-Prv	Na-carb
P (GPa):	8	13	8	23.5	16	22	22	22	22	18
T (°C):	900	1125	900	1400	1350	1400	1400	1300	1300	1200
SiO ₂ (wt %)	54.83	63.21	65.92	53.24	60.02	41.66	35.00	50.29	4.09	0.19
TiO ₂	-	-	0.08	-	0.10	0.72	1.27	0.10	28.91	0.01
Al ₂ O ₃	21.74	18.47	19.64	30.45	23.54	21.24	46.94	0.15	6.79	0.12
FeO	2.69	0.62	0.30	1.48	1.16	17.04	1.87	0.26	53.41	6.86
MgO	2.34	0.05	0.00	0.11	0.85	6.53	0.23	0.06	0.99	3.79
CaO	1.48	0.58	0.16	0.84	1.68	10.89	11.96	46.62	0.61	36.93
Na ₂ O	0.05	0.41	0.00	0.20	12.36	1.17	0.50	0.12	0.64	10.54
K ₂ O	13.51	15.56	15.94	12.92	0.11	0.36	1.54	0.09	0.38	0.59
H ₂ O _{calculated}	4.47	0.00	-	n.a.	-	-	-	-	-	-
CO ₂ *	0.00	0.00	0.00	0.00	0.00	0.00	0.00	0.00	0.00	40.98
Total	101.10	98.90	102.04	99.25	99.82	99.61	99.31	97.69	95.83	100.00
Si (a.p.f.u.)	3.68	2.96	2.99	2.96	2.02	3.16	2.25	0.99	0.10	0.00
Ti	-	-	0.00	-	0.00	0.04	0.06	0.00	0.53	0.00
Al	1.71	1.02	1.05	1.99	0.94	1.90	3.56	0.00	0.19	0.00
Fe _{tot}	0.15	0.20	0.01	0.07	0.03	1.08	0.10	0.00	1.08	0.09
Mg	0.23	0.00	0.00	0.01	0.04	0.74	0.02	0.00	0.04	0.09
Ca	0.11	0.03	0.01	0.05	0.06	0.88	0.82	0.99	0.02	0.64
Na	0.01	0.04	0.00	0.02	0.81	0.17	0.06	0.00	0.03	0.17
K	1.15	0.93	0.92	0.92	0.00	0.03	0.13	0.00	0.01	0.00
Tot.	7.05	5.00	5.00	6.01	3.91	8.00	7.00	2.00	2.00	1.00
Mg-no.(Fe _{tot}) (molar)	60.5	0.00	0.00	12.5	57.1	40.7	16.7	0.00	3.57	50.0
No. oxygens for norm	12	8	8	9	6	12	11	3	3	6
No. OH-site	2			1						

Complete dataset of mineral compositions can be found in the online Supplementary Data.

*CO₂ content calculated by difference of 100 and the measured analytical total.

Carbonates stable in the different experiments are Mg-calcite in the AM composition (Thomsen & Schmidt, 2008) and dolomite–ankerite solid solution in the DG2 composition at $P \leq 6.5$ GPa. From 8 to 16 GPa (i.e. as long as cpx is stable in the subsolidus) ferroan magnesite + aragonite coexist, but at ≥ 16 GPa magnesite coexists with a Na-rich calcite. Mg-calcite contains up to 14 and 16 mol % siderite and magnesite at subsolidus conditions, and dolomite contains 17 and 35 mol % siderite and magnesite, respectively. Both are replaced by pure aragonite + ferroan magnesite at 8 GPa, the latter with 10 mol % calcite and a Mg-number of 57.9 (DG2). At 16 GPa (1300°C), Na-rich calcite (16–18 mol % Na₂CO₃, 60–68 mol % CaCO₃) replaces aragonite and coexists with ferroan magnesite, the latter with 4–6 mol % calcite and a Mg-number of 71.1 (DG2). Ferroan magnesite coexisting with Na-rich carbonate has a significantly higher Mg-number than when coexisting with aragonite (55.6 instead of 32.6 in

the AM composition, and 71.1 instead of 57.9 in the DG2 composition, Figs 6 and 7). In the DG2 composition at 22 and 23.5 GPa, and temperature $\leq 1400^\circ\text{C}$, a third carbonate with *c.* 20 wt % Na₂O (33–34 mol % Na₂CO₃) but almost no Fe and Mg (<1 mol %) has been identified (Fig. 3h). Texturally, this carbonate forms intergranular, irregular-shaped needles contrasting with the rhombohedral habit of both the Ca-carbonate with ~ 10 wt % Na₂O and magnesite. We interpret this additional Na-rich carbonate as a quench product from the fluid.

Phengite (Phen) has been found only at $P \leq 8$ GPa at subsolidus or near-solidus conditions in the hydrous AM composition. As expected, a trend of increasing celadonite content or inverse Tschermak's substitution with pressure, from 3.1 Si p.f.u. at 2.5 GPa to 3.68 Si p.f.u. at 8 GPa, is observed (Thomsen & Schmidt, 2008; Grassi & Schmidt, 2011).

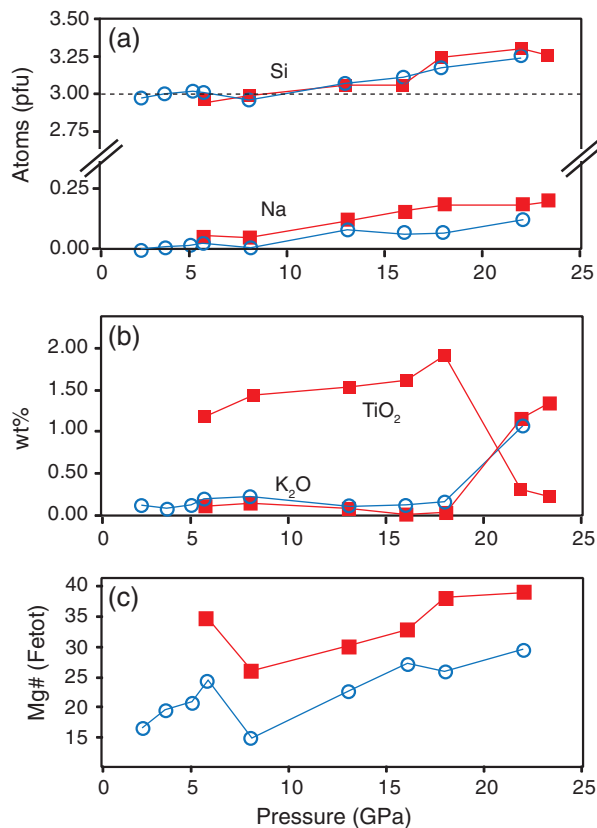


Fig. 4. Composition of garnet as a function of pressure. At subsolidus conditions garnets in both compositions are similar. The increase in Si (a) is not due to a Tschermaks type majorite component, which remains below detection limit in the kyanite/corundum-saturated bulk compositions, but to a charge-coupled substitution $M^{2+} + Al = (Na, K) + (Si, Ti)$. \circ , 1.1 wt % H₂O AM composition; \blacksquare , dry DG2.

K-hollandite (K-holl) contains a few weight per cent Na₂O and CaO, mostly increasing with temperature and especially with pressure. In the DG2 composition (3.2 wt % bulk Na₂O) Na in K-hollandite increases steadily with pressure, whereas in the AM composition (2.4 wt % bulk Na₂O) Na in K-hollandite reaches a maximum at 16 GPa (0.06 Na p.f.u.) and then remains constant with further increasing pressure. The different behaviour of sodium in the AM composition can be explained by the lower bulk Na₂O in combination with H₂O, part of the Na being more easily accommodated in a Na-rich fluid. Ca in K-hollandite increases in the DG2 composition from 0.03 to 0.08 Ca p.f.u. at 13–22 GPa. In the AM composition, Ca in K-hollandite is constant at ~0.05 p.f.u. At 16 and 18 GPa, K-hollandite in the AM composition shows a Si deficit up to 0.15–0.2 a.p.f.u. at the lowest temperatures. This deficit may be attributed to the incorporation of small amounts of hydrogen owing to the substitution of Si by Al + H on the octahedral site, as is well known from

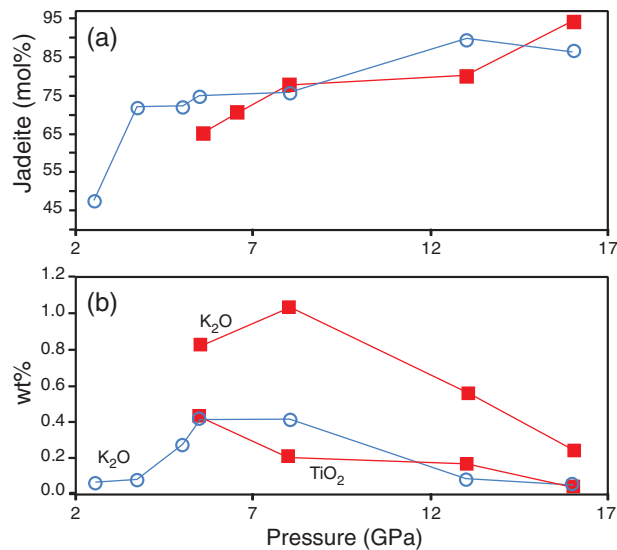


Fig. 5. Clinopyroxene composition as a function of pressure. (a) Jadeite (mol %) component increases with pressure; (b) variation of K₂O and TiO₂; the maximum K₂O content of cpx is attained at 8 GPa (i.e. at a pressure just below the formation of K-hollandite). A similar trend is also observed for the K content of carbonate melts (see Figs 8 and 9). \circ , 1.1 wt % H₂O AM composition; \blacksquare , dry DG2.

stishovite (Panero *et al.*, 2003; Panero & Stixrude, 2004; Litasov *et al.*, 2007). The possible presence of hydrogen is also indicated by low totals (94–98 wt %) in some analyses.

In the hydrous AM composition at 22 and 23.5 GPa, at the lowest temperatures, K-hollandite is replaced by a potassium phase with higher Al₂O₃ contents, and a K:Al:Si ratio of *c.* 1:2:3, here termed the HPK phase. The absence of this phase in the dry DG2 experiments suggests some structural water, yielding the most simple approximate formula KAl₂Si₃O₉(OH). Raman spectra of this phase are similar to those of K-hollandite with characteristic bands near 760 and 217 cm⁻¹ (Liu & El Gorse, 2007) suggesting some structural similarities between both potassium phases. Analyses, Raman spectra and BSE images are given in the Supplementary Data (available at <http://www.petrology.oxfordjournals.org>).

Coesite (Coe), present at ≤ 8 GPa and verified by Raman spectroscopy, is almost pure in composition. Its composition clearly differs from that of stishovite (Sti), present at ≥ 13 GPa, which contains up to 2.3 wt % of Al₂O₃ and 0.77 wt % of FeO_{tot}, both generally increasing with pressure.

Kyanite (Ky) and corundum (Crn) have FeO_{tot} contents of up to 3 wt %, and TiO₂ and MgO up to 0.5 wt %. Corundum contains up to 2 wt % SiO₂. These minor oxide components generally increase with pressure and temperature.

The CAS phase (CaAl₄Si₂O₁₁) (Gautron *et al.*, 1997) is stable only at $P \geq 22$ GPa at temperatures above the solidus

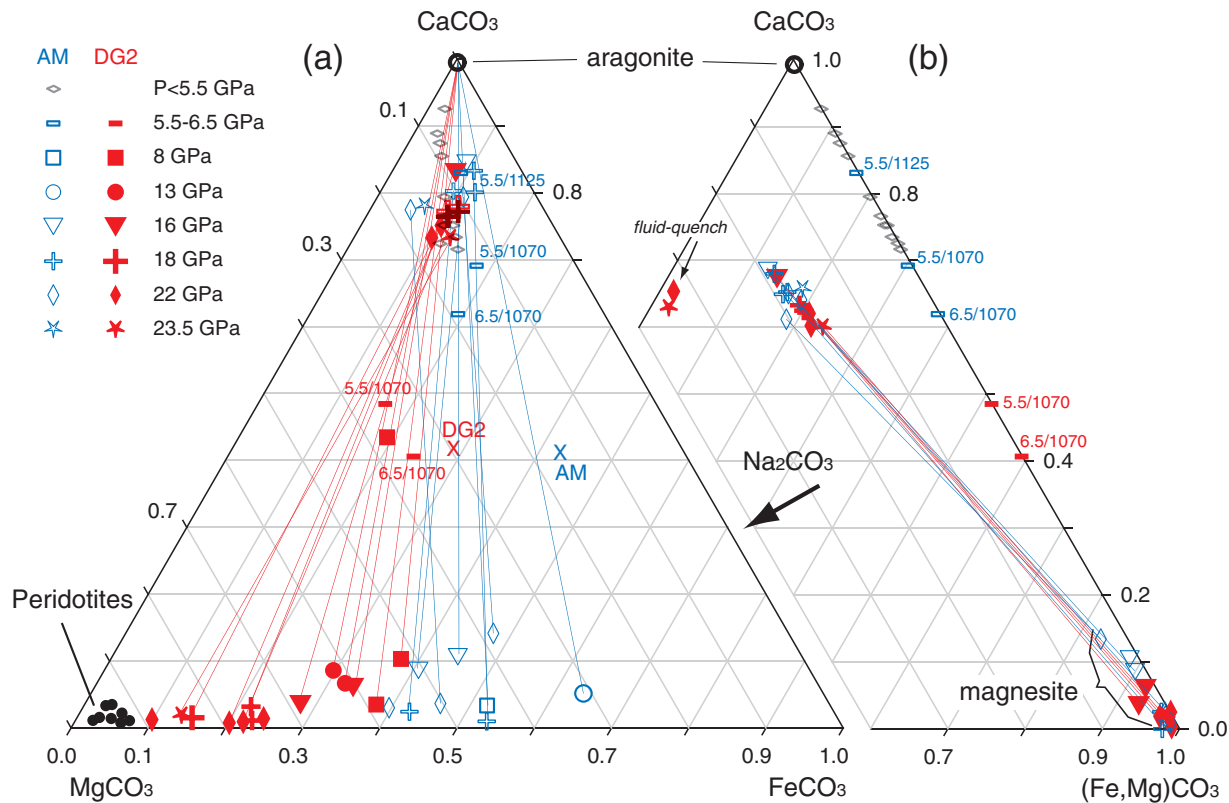


Fig. 6. Carbonate compositions in (a) CaCO_3 - MgCO_3 - FeCO_3 and (b) CaCO_3 - Na_2CO_3 - $(\text{Mg,Fe})\text{CO}_3$ space. The Mg-number of magnesite increases with pressure whereas the Na-carbonates show an increase in $(\text{Mg,Fe})\text{CO}_3$ component with pressure. The almost Mg- and Fe-free Na-carbonate is interpreted as a quench from an Na-rich fluid. Aragonite remains pure CaCO_3 in all experiments. The strong positive correlation between magnesite composition and the Mg-number of the related bulk composition should be noted. x, bulk compositions.

(1400°C), in agreement with the results of Ishibashi *et al.* (2008). A simplified formation reaction is $1 \text{ Ca-perovskite} + 2 \text{ corundum} + 1 \text{ stishovite} = 1 \text{ CAS}$. The CAS phase contains up to 14 wt % TiO_2 in DG2, and is an important host for alkalis, with up to 3.9 wt % K_2O and 0.7 wt % of Na_2O at the highest temperatures. The excess of SiO_2 and alkalis and the deficit of Al_2O_3 with respect to the ideal stoichiometry indicate coupled substitutions of the type $\text{Al}_3\text{Si}_2(\text{Na,K})$ and $\text{Ca}_{-1}\text{Al}_{-1}\text{Si}(\text{Na,K})$, as already recognized by Hirose & Fei (2002) and Zhai & Ito (2008) in K-free sodic systems.

Ca(Ti)-perovskite (Prv) crystallizes at $P \geq 22$ GPa at low temperatures. At subsolidus conditions it coexists with Ti-rich Fe-perovskite (DG2). At higher temperature, after the breakdown of the latter, Ca-perovskite contains up to 27 wt % of TiO_2 (DG2). Being Ti-rich, this Ca-perovskite is quenchable and does not transform to an amorphous substance as does near endmember Ca-perovskite (Leinenweber *et al.*, 1995).

Fe(Ti)-perovskite is stable only at $P \geq 22$ GPa at subsolidus conditions; its amount increases with pressure and decreases with increasing temperature. In the hydrous

Ti-free composition, Fe-perovskite is almost pure in composition, with only 1.5 wt % Al_2O_3 . In the anhydrous Ti-bearing system (DG2), Fe-perovskite contains up to 39 wt % TiO_2 .

Oxides are Ti-oxides (rutile II, TiO_2 with α - PbO_2 structure) at 8 and 13 GPa in the DG2 composition and an almost pure iron oxide with ~ 3 wt % Al_2O_3 in the hydrous AM composition at $P > 20$ GPa. Unfortunately, this latter phase is too small ($< 1-2 \mu\text{m}$) to be accurately analyzed by micro-Raman spectroscopy.

Melt compositions

At the pressures of this study (i.e. 5.5–22 GPa) all melts are magnesio- (DG2) to ferro-dolomitic (AM) carbonate melts containing large amounts of alkalis (Figs 8 and 9). At 5.5–13 GPa, the first melts are potassium-rich carbonate melts with a maximum K_2O content and K/Na ratio at the phengite or Kfs to K-hollandite reaction at 8 GPa. At 6.5 GPa, 1070°C, the first carbonate melt in the AM composition coexists with small amounts of Kfs and Mg-calcite, whereas in the DG2 composition Kfs does not

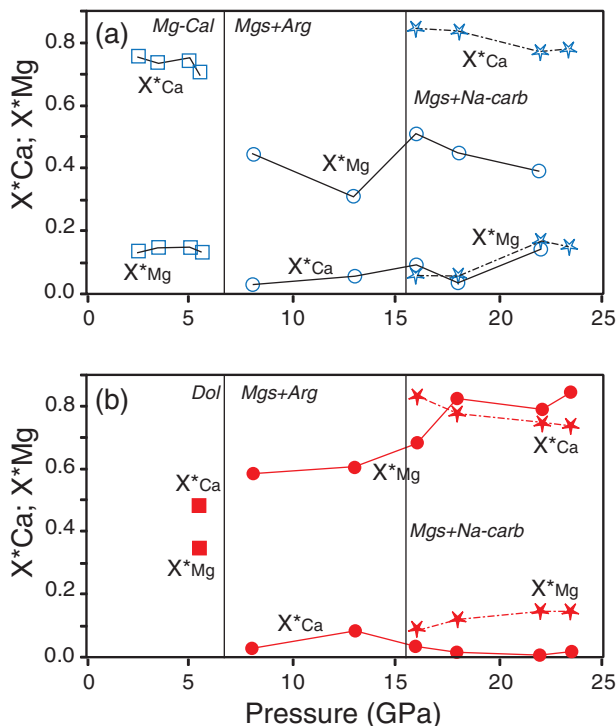


Fig. 7. X^*_{Ca} [$Ca/(Mg + Fe + Mg)$] and X^*_{Mg} [$Mg/(Mg + Fe + Mg)$] of carbonates crystallizing in (a) the AM and (b) the DG2 bulk compositions as a function of pressure. Squares are for ferroan dolomite or Mg-calcite at <7 GPa, circles for ferroan magnesite at ≥ 8 GPa and stars are for Na-carbonates at ≥ 16 GPa.

coexist with melt. As the AM composition contains 1.1 wt % H_2O , which should destabilize Kfs with respect to the dry DG2 composition, the absence of Kfs in DG2 is most probably due to its lower bulk K_2O content. With further increase in pressure, melts remain carbonatitic but gradually change from potassium-rich at 8 GPa to sodium-rich at 22 GPa (Table 1). This is due to an increasing compatibility of potassium in K-hollandite with pressure, a continuous decrease of $D_{Na}^{cpx/melt}$ from 8 to 16 GPa and the disappearance of cpx near 16 GPa. The K_2O/Na_2O weight ratio in the carbonate melt (Fig. 10) decreases from 41 at 8 GPa to 0.14 at 22 GPa. The K/Na ratio in melts from the AM composition is always slightly higher than in melts from the DG2 composition, owing to a higher bulk K_2O and lower Na_2O concentrations in the AM bulk. At the cpx-out reaction at 16 GPa/1300°C, the melts have a K_2O/Na_2O weight ratio of approximately unity, defining the upper pressure limit for potassic melts and potassic metasomatism (Fig. 10). In both compositions X^*_{Ca} in the carbonate melt increases with pressure from 0.57–0.62 at 8 GPa to 0.71 at 16 GPa. With further pressure increase, X^*_{Ca} in the carbonate melts decreases to 0.49–0.56 at 22 GPa. X^*_{Mg} in the AM composition shows a constant increase with pressure from 0.1 at 8 GPa to 0.23 at 22 GPa. In the DG2 composition, X^*_{Mg} is 0.16 at 8 GPa and 0.33 at 22 GPa (Fig. 9a). SiO_2 and Al_2O_3 concentrations of all near-solidus melts from 5 to 22 GPa are low (i.e. below 1.2 and 1.8 wt %, respectively).

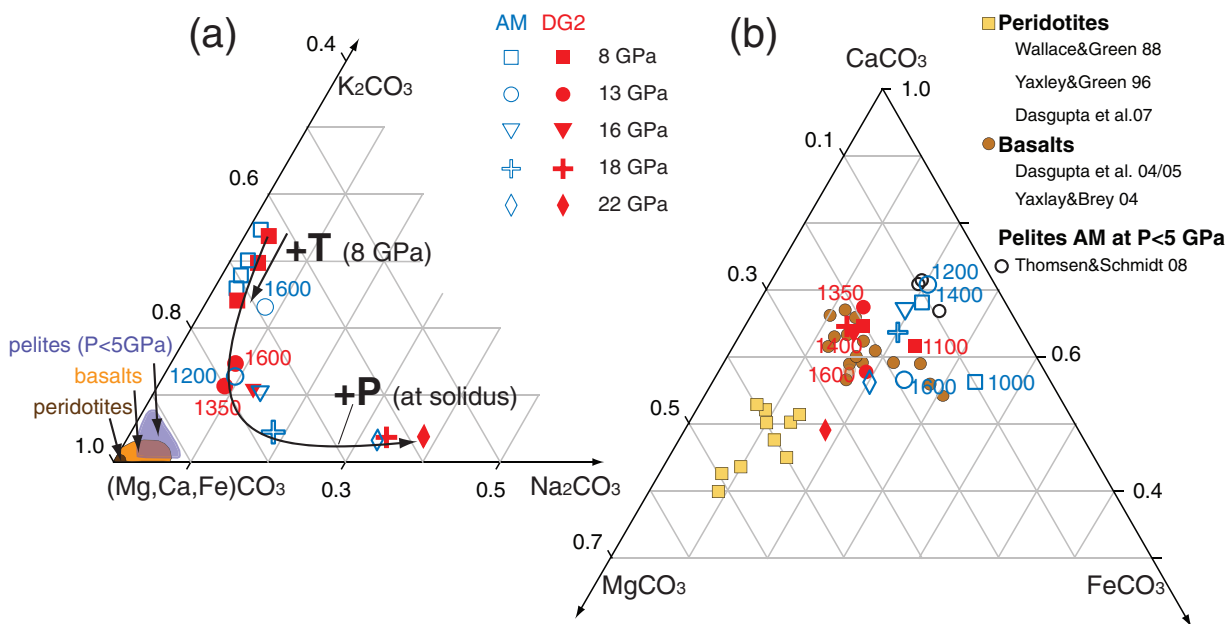


Fig. 8. (a) Composition of carbonate melts projected into Na_2CO_3 – K_2CO_3 – $(Mg, Ca, Fe)CO_3$ space. As is to be expected, carbonate melts formed from pelites have higher K_2CO_3 and Na_2CO_3 components than those from carbonated basalts and peridotites. From 8 to 22 GPa the potassium content decreases whereas the sodium content increases. (b) Compositions of carbonate melts projected into $FeCO_3$ – $CaCO_3$ – $MgCO_3$ space. Projected from alkalis, carbonate melts from pelites plot in the same area as carbonate melts from carbonated basalts, which have similar bulk X^*_{Ca} and X^*_{Mg} . From 16 to 22 GPa an increase of the $MgCO_3$ and a decrease of $CaCO_3$ component is observed.

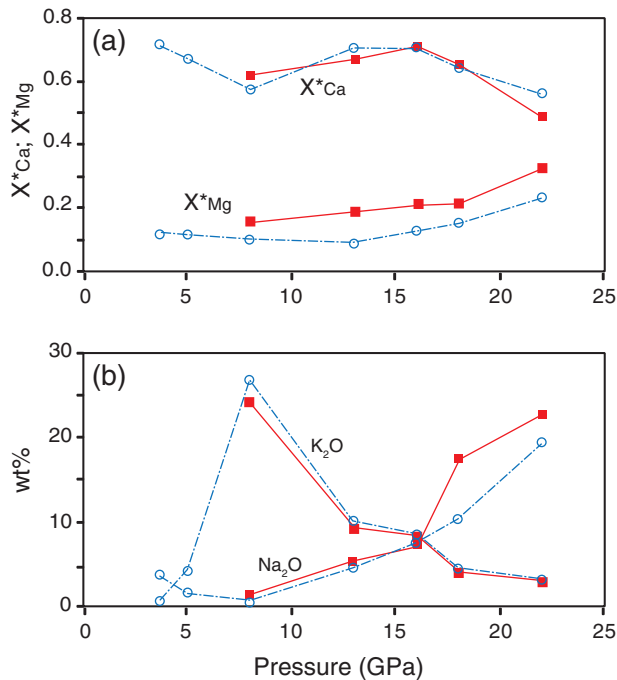


Fig. 9. (a) X^*_{Ca} and X^*_{Mg} as function of pressure for the pelite-derived carbonate melts. (b) Melt K_2O and Na_2O contents (in wt %) as a function of pressure. At 8 GPa carbonate melts are highly potassic but become more enriched in Na_2O with increasing pressure, in particular after the breakdown of cpx (16 GPa/1300°C). The decrease in melt K_2O with pressure is related to the increasing stability of K-hollandite. ○, 1.1 wt % H_2O AM composition; ■, dry DG2.

DISCUSSION

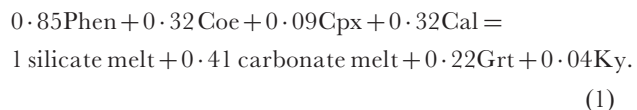
Melting behavior

The position and shape of the solidus from 2 to 24 GPa (Fig. 1) depends mostly on the stability and composition of the hydrous and carbonate phases, on the presence of a fluid, and on the (in-)compatibility of alkalis with the various alkali-rich subsolidus phases such as phengite, Kfs, K-hollandite, clinopyroxene and carbonates. Thomsen & Schmidt (2008) determined that melts generated at the solidus at $P \leq 5$ GPa are silicate melts with a peraluminous potassic granite composition at 2.5 GPa, gradually changing to a slightly peralkaline phonolite composition at 3.7–5 GPa. The decrease of SiO_2 content with increasing pressure is related to an increase in the CO_2 solubility of the melt (Thomsen & Schmidt, 2008). The increasingly potassic character with increasing pressure is a consequence of the increasing compatibility of Na owing to an increasing jadeite content in cpx (Schmidt *et al.* 2004), an effect that is amplified by the presence of CO_2 . Between 5 and 5.5 GPa the carbonate melting reaction crosses the fluid-absent silicate solidus, leading to carbonate melts at the solidus at >5 GPa. Below we discuss the melting reactions and their character in terms of fluid-absent or

fluid-present behaviour from 3.5 to 22 GPa. The melting reaction stoichiometry is derived from mass balancing educts and products taken from the highest temperature subsolidus and the lowest temperature supersolidus experiment, respectively.

In the hydrous AM composition, melting is fluid-absent to 9 GPa; that is, as long as phengite is stable (Fig. 1). At higher pressures, the absence of any hydrous phase suggests the presence of a fluid phase; the apparent solidus is then established by the appearance of the first quenched carbonate melts. In the nominally anhydrous composition DG2, the presence of a liquid at temperatures lower than carbonate melt formation is indicated by mass-balance calculations and textures at $P > 16$ GPa; that is, after the breakdown of cpx (16 GPa/1300°C). Above this pressure, the apparent solidus is again defined by the appearance of the first quenched carbonate melts.

At pressures from 2.5 to 3.5 GPa the melting out of coesite and phengite at 920–1000°C is responsible for the generation of 30–35 wt % silicate melt coexisting with Mg-calcite in the H_2O -bearing AM composition (Thomsen & Schmidt, 2008). From 3.5 to 5 GPa, a silicate melt coexists with a carbonate melt over a limited temperature interval around 1100°C (Figs 1 and 11). At 5 GPa, the melting reaction produces a silicate and a carbonate melt through the reaction



For the dry DG2 composition, there are no experiments available at $P < 5.5$ GPa, but recently Tsuno & Dasgupta (2010) showed that the solidus of a dry carbonated eclogitic pelite at 2.5–3 GPa locates at *c.* 950°C. Similar to the $H_2O + CO_2$ -bearing but fluid-absent AM composition, the first melt of the CO_2 -only Tsuno & Dasgupta composition is a K-rich granite melt. This melt forms *c.* 200°C below the solidus of H_2O - and CO_2 -free pelite (Spandler *et al.*, 2010) and coexists with carbonate minerals for up to 100°C above the solidus. The expected relative sequence in melting temperatures is volatile-free pelite $>$ CO_2 -bearing pelite $>$ $CO_2 + H_2O$ -bearing pelite. This sequence is maintained, but there is a surprisingly small difference of $<30^\circ\text{C}$ between the melting temperatures of the latter two. Our $CO_2 + H_2O$ -bearing pelite differs from the 10–90 composition of Tsuno & Dasgupta (2010, table 1) by a lower X_{Mg} (0.28 vs 0.41), higher alkali contents (2.4 and 3.6 wt % Na_2O and K_2O vs 2.3 and 2.0 wt % Na_2O and K_2O) and a similar X_{Ca} (0.71 vs 0.70), thus the similar melting temperatures remain difficult to explain. On the other hand, the large difference in melting temperature between the volatile-free pelite of Spandler *et al.* (2010) and the CO_2 -only pelite of Tsuno & Dasgupta (2010) points to

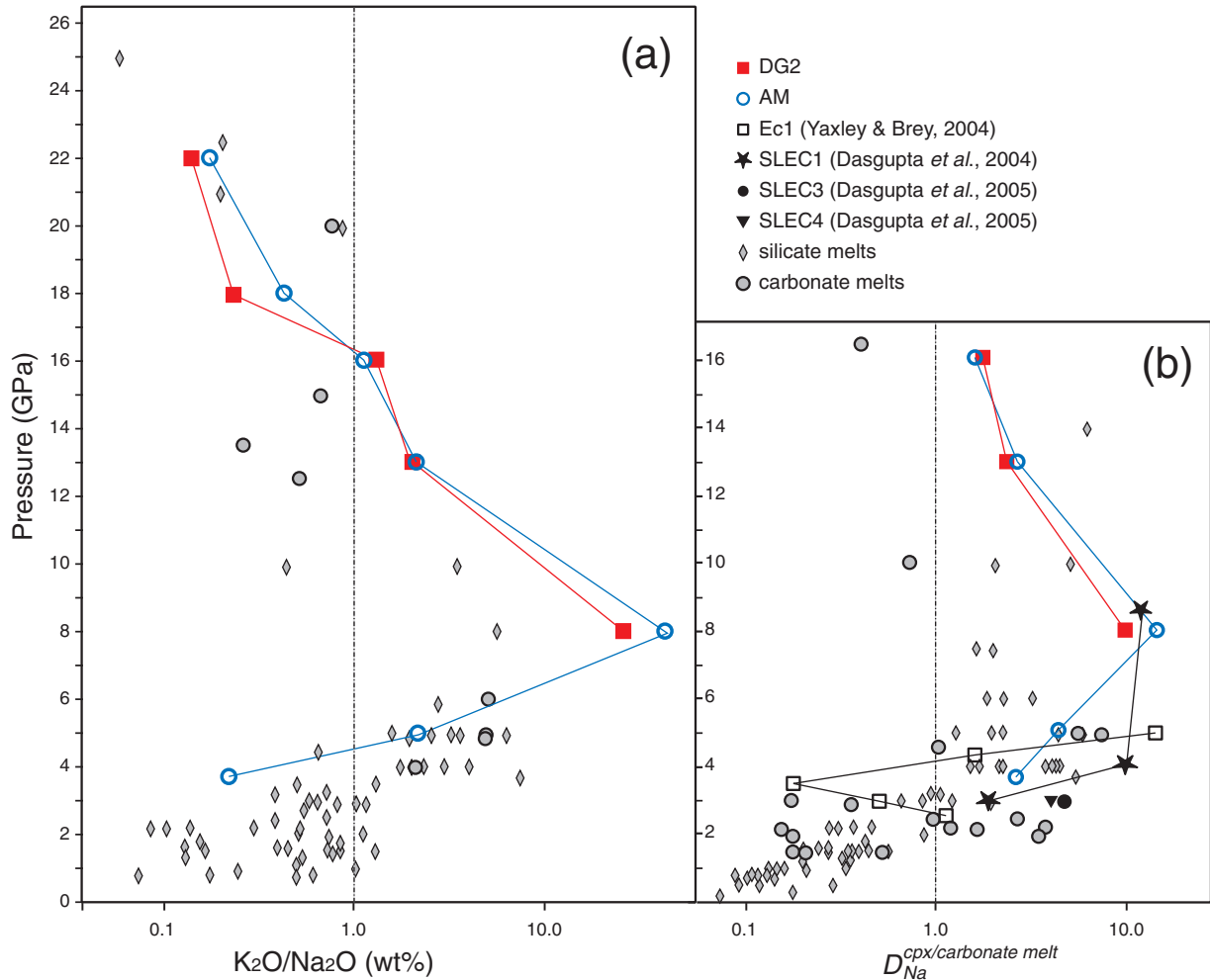


Fig. 10. (a) K_2O/Na_2O weight ratios vs pressure in carbonate melts, illustrating a pressure window for ultrapotassic melts and metasomatism between 5 and 15 GPa with a K_2O/Na_2O maximum near the phengite/Kfs breakdown at 9 GPa. This pressure interval correlates well with the highest sodium partition coefficients between cpx and melt illustrated in (b). The breakdown of jadeitic cpx at 16 GPa leads to sodic dolomite-carbonate melts at higher pressures. (b) $D_{Na}^{cpx/melt}$ vs pressure, illustrating the increase in compatibility of Na in cpx with increasing pressure up to a cpx/carbonate melt partition coefficient of 18 at 8 GPa, followed by a decrease to values of $c. 2-2.5$ at 13 GPa and 1.7 at 16 GPa when approaching the cpx pressure stability. It should be noted that in some of the reported studies, the compositions of the carbonate melts were not the main focus and that Na_2O concentrations in tiny melt pools are not reliably measurable. Thus, several of the plotted partition coefficients are likely to represent underestimations. Plotted silicate melt alkali ratios and cpx/silicate melt partition coefficients are from the data of Irifune *et al.* (1994), Yasuda *et al.* (1994), Blundy *et al.* (1995), Rapp & Watson (1995), Singh & Johannes (1996), Wang & Takahashi (1999), Schmidt *et al.* (2004), Kessel *et al.* (2005), Hermann & Spandler (2008) and Spandler *et al.* (2010). Data for carbonate melts are from Wallace & Green (1988), Ryabchikov *et al.* (1989), Brenan & Watson (1991), Thibault *et al.* (1992), Dalton & Wood (1993), Sweeney *et al.* (1995), Blundy & Dalton (2000), Yaxley & Brey (2004), Dasgupta *et al.* (2004, 2005), Dasgupta & Hirschmann (2006), Ghosh *et al.* (2009) and Litasov & Ohtani (2009).

the crucial role of CO_2 in lowering the solidus through dissolution in granitic melts at these pressures.

In contrast to the melts at <5 GPa, the first melts are carbonate melts at ≥ 5.5 GPa. The first small amounts of these carbonate melts just above the solidus appear concomitantly with the destabilization of phengite and the formation of Kfs. The formation of a carbonate melt and the progressive dissolution of potassium in this melt, destabilizing phengite and Kfs, leads to the disappearance of the

classical melting reaction phengite/Kfs + quartz/coesite = silicate melt + kyanite + garnet. At 5.5 GPa and 1180°C, $c. 100^\circ C$ above the solidus, the carbonate melts are highly potassic with only minor amounts of Al_2O_3 (3 wt %) and SiO_2 (4 wt %).

In the simple $K_2O-Al_2O_3-SiO_2$ system, Kfs is stable to 6 GPa, where it reacts to wadeite ($K_2Si_4O_9$) (Yong *et al.*, 2006), kyanite and coesite. Wadeite is then stable to 9–10 GPa and is replaced by K-hollandite at higher

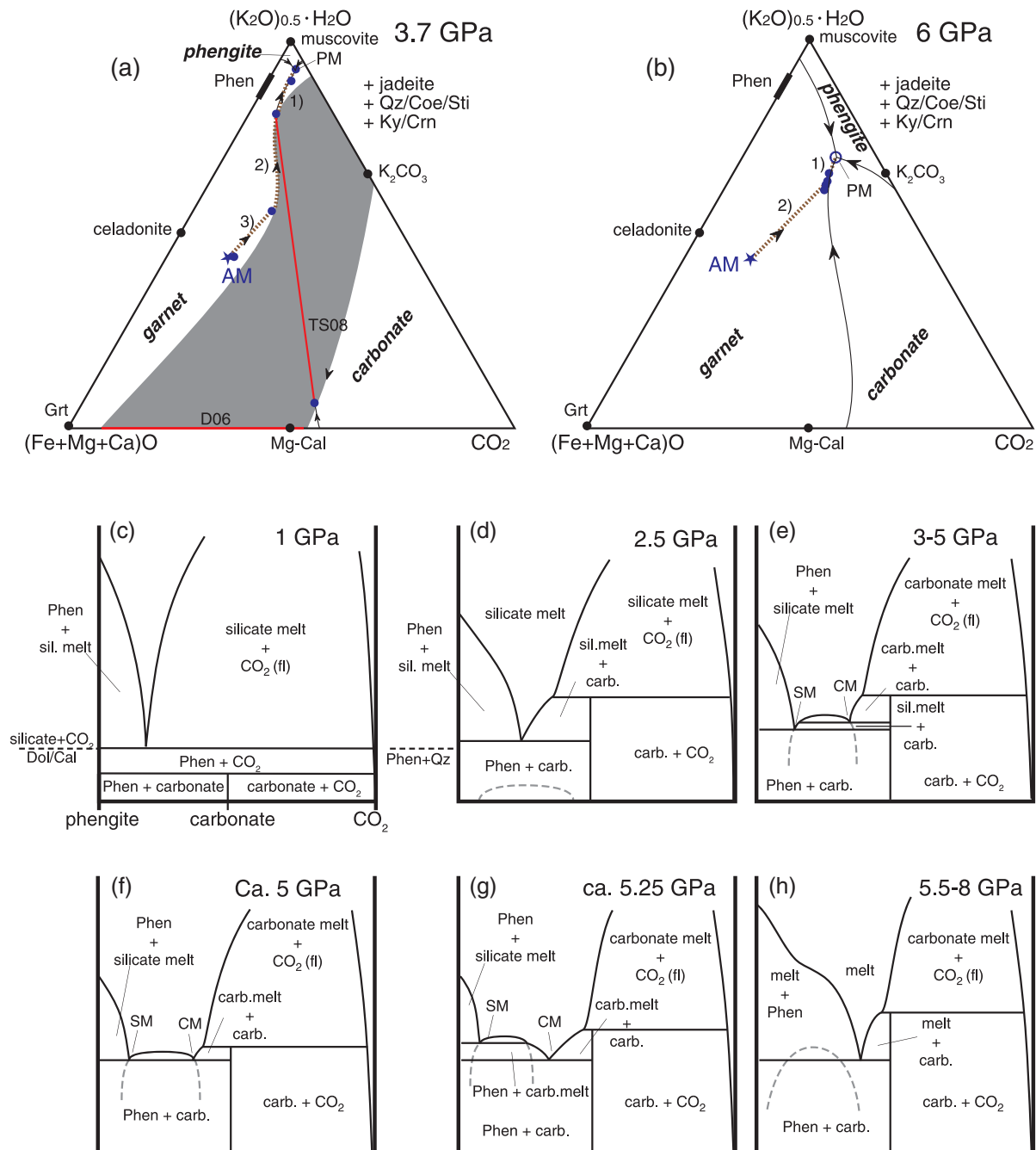
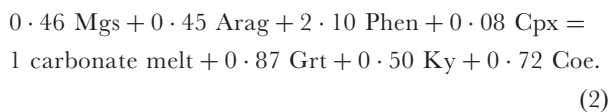
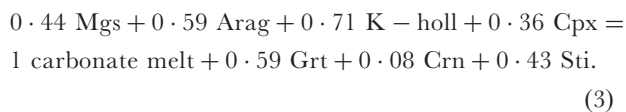


Fig. 11. Principal melting topology of silicate-carbonate-CO₂ systems in projection from coesite, kyanite and jadeite into CO₂-(K₂O)_{0.5}·H₂O-(Fe,Mg,Ca)O at (a) 3.7 GPa (Thomsen & Schmidt, 2008) and (b) 6 GPa with analyzed melt compositions, melt surface, peritectic points and curves. This projection would be thermodynamically valid if (K₂O)_{0.5}+H₂O were a system component and if Ca + Mg + Fe²⁺ mixed ideally. Bold italic labels designate liquidus surface phases. Thick dotted brown lines represent melt paths of our bulk compositions with increasing temperature. The peritectic minimum (PM) moves from the (K₂O)_{0.5}·H₂O corner towards more M²⁺+CO₂-rich compositions after the crossing of the carbonate melting reaction and the fluid-absent silicate solidus between 5 and 5.5 GPa. (a) At 3.7 GPa phengite is exhausted at the peritectic and melt develops from the peritectic point (PM) along the garnet-carbonate cotectic until this cotectic intersects the carbonate-silicate melt immiscibility gap (grey field). The tie-line and width of the immiscibility gap along the (Fe + Mg + Ca)O-CO₂ line is after Dasgupta *et al.* (2006) (D06). At 3.7 GPa, Mg-calcite melts in a monotectic yielding a carbonate melt. The two melt compositions then evolve along the limits of this solvus (2) until carbonate melt is exhausted and then the melts proceed on the garnet liquidus surface. (b) At 6 GPa at the peritectic (PM), phengite is exhausted leading to a carbonate melt that evolves along the garnet-carbonate cotectic (1) until carbonate minerals are exhausted. At this pressure no liquid immiscibility was observed. (c-h) Melting relations in *F-X* pseudo-binaries along phengite-CO₂ in the same system as (a) and (b) additionally projected from garnet. This series of pseudo-binaries illustrates the main features of melting and decarbonation in sedimentary systems: (c) breakdown of carbonates before reaching the silicate solidus; (d) silicate melting leaving residual carbonate; (e) the intersection of the immiscibility gap with the silicate solidus producing a carbonate mineral to carbonate melt monotectic and coexisting silicate (SM) and carbonate melt (CM); (f) the precise pressure at which the silicate and carbonate melting reactions occur at the same temperature; (g) carbonate melting at the solidus and a very limited coexistence of carbonate with silicate melts; (h) liquid immiscibility again metastable; a continuum from carbonate to silicate melts forms. The dashed line indicates metastable parts of the immiscibility gap.

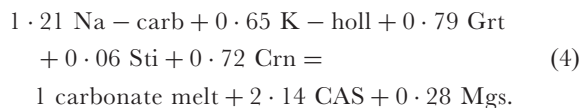
pressures. In natural or more complex systems such as our simplified pelitic system, wadeite has never been observed. Our experiments yield Kfs to 8 GPa, probably stabilized with respect to wadeite by Na and Fe³⁺. Notably, in the pressure range of 6–9 GPa, where wadeite would occur in the simple system, solidus temperatures are relatively low compared with lower and higher pressures. Reaction (2) illustrates the melting behaviour at 8 GPa for the hydrous composition AM:



At around 9 GPa phengite reacts to form K-hollandite, which is then responsible for the increased compatibility of potassium with pressure and the subsequent shift of the solidus towards higher temperatures in both compositions. With increasing pressure cpx begins to play a major role in the melting reaction, resulting in carbonate melts with a higher sodium content and lower K/Na ratio. At 13 GPa the melting reaction is



Before reaching 16 GPa, a strong decrease of the solidus temperature in the dry composition DG2 occurs concomitantly with the progressive breakdown of cpx (16 GPa, 1300°C) and the crystallization of a Na-rich Ca-carbonate. As indicated by the deficit of Na in the equilibrium minerals and by the concentration of Na along grain boundaries, the Na-rich Ca-carbonate coexists with a Na- and CO₂-rich fluid. This transition from fluid-absent to fluid-saturated would explain the observed 50°C decrease in the solidus temperature near 16 GPa in the dry DG2 composition. At pressures beyond the stability of cpx, both the dry and H₂O-bearing compositions show the first appearance of carbonate melt at the same temperature, a further indication of fluid-saturation in both compositions. At $P > 16$ GPa, the solidus temperature again increases with pressure, the melting reaction is dominated by the Na-rich carbonate and in minor amounts by K-hollandite. This yields carbonate melts with low K/Na ratios, further decreasing with pressure. At 22 GPa, melting also involves the crystallization of the CAS phase:



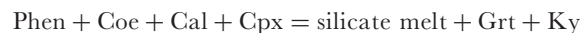
For the melting reaction at 22 GPa, the involvement of perovskite cannot be constrained by mass balance, owing to its small amount at near-solidus conditions. With

increasing temperature, perovskites are replaced by garnet and the CAS phase.

The melting diagram of carbonated sedimentary systems

The principal melting topology of silicate–carbonate–CO₂ systems in projection from coesite, kyanite and jadeite is illustrated in Fig. 11a and b for 3.7 and 6 GPa. To allow for projection into a ternary, we have reduced (Ca,Mg,Fe²⁺)O to one component, yielding the three-component system CO₂–(K₂O)_{0.5}–H₂O–(Fe,Mg,Ca)O. This projection would be thermodynamically valid if (K₂O)_{0.5}+H₂O were a system component (i.e. if the K/H ratio were the same in all phases, in this case mica and melt) and if Ca+Mg+Fe²⁺ mixed ideally. In Fig. 11a and b, we plotted melt compositions at 3.7 GPa from Thomsen & Schmidt (2008), from this study at 6 GPa, and from Dasgupta *et al.* (2006) at 3 GPa for the K-free MORB+CO₂ system (where MORB is mid-ocean ridge basalt), which locates at the (Mg+Fe+Ca)O–CO₂ baseline of the ternary.

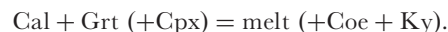
At 3.7 GPa, a peritectic minimum (PM) occurs near the (K₂O)_{0.5}–H₂O corner, and melting takes place through the reaction



(Thomsen & Schmidt, 2008). At higher pressures, the minimum PM moves towards more M²⁺+CO₂-rich compositions, and at 6 GPa melting occurs through



At temperatures above the peritectic, melts evolve along garnet–carbonate cotectic (1) in Fig. 11a and b. By plotting the effectively measured melt compositions and from mass balance this cotectic appears to be congruent in the projection of Fig. 11a and b, yielding a melting reaction



The complexity of this system lies in the fact that at low pressure (e.g. 2.5 GPa) only silicate melt occurs with some carbonate component dissolved, whereas at high pressure (e.g. 8 GPa) only carbonate melt occurs. The carbonate melts gradually dissolve silicate components, reaching 5.5 wt % SiO₂ at 400°C above the solidus temperature (at 8 GPa, Fig. 1). At intermediate pressures (i.e. 3–5 GPa), coexisting immiscible silicate and carbonate melts are observed (Thomsen & Schmidt, 2008). Thus, at 3.7 GPa, the garnet–carbonate cotectic intersects the silicate–carbonate miscibility gap, and carbonates melt at a monotectic, yielding a carbonate liquid. The two melt compositions then evolve along the limits of this solvus [for the silicate melt (2)] in Fig. 11a until the carbonate melt is exhausted, and melts proceed on the garnet liquidus surface [along (3) in Fig. 11a]. At 6 GPa (Fig. 11b), the first

measured liquid near PM is a carbonate melt forming through the peritectic melting reaction (2), which may produce a minor amount of garnet. Again, phengite is consumed at the peritectic PM. With increasing temperature, the next phase to be consumed is Mg-calcite along the cotectic (1) in Fig. 11b. When Mg-calcite melts out, melts leave the garnet-carbonate cotectic and evolve towards garnet on the liquidus surface. At 6 GPa, no liquid immiscibility was observed.

The development from silicate to carbonate melt at the solidus can best be understood by visualization of the melting relations (Fig. 11c–h). This series of pseudo-binary T - X sections along phengite-CO₂ (Fig. 11a and b) is projected from garnet in addition to jadeite, kyanite and coesite/quartz, leaving phengite on the left-hand side of these pseudo-binaries. Although these diagrams involve major simplifications, they illustrate well the decarbonation and melting relations of carbonated pelites, which yield silicate melts coexisting with carbonates at low pressure, two melts at intermediate pressure, and carbonate melts at high pressure. The sequence of diagrams illustrates: (1) the breakdown of carbonates before reaching the silicate solidus at the lowest pressure (Fig. 11c); (2) silicate melting in the presence of carbonates and a hypothetical occurrence of a metastable immiscibility gap between silicate and carbonate melts (Fig. 11d); (3) the intersection of the immiscibility gap with the silicate solidus (Fig. 11e), resulting in a monotectic where carbonate + silicate melt react to carbonate melt in addition to the silicate eutectic; (4) the pressure at which the eutectic and (former) monotectic occur at the same temperature (Fig. 11f). This pressure corresponds to the intersection of the silicate melting and carbonate melting reactions in P - T space, as occurring in the AM composition just above 5 GPa. At higher pressures (Fig. 11g), melting at the solidus now results first in a single carbonate melt. This carbonate melt may coexist with silicate melt over a narrow temperature range. When pressure increases to ≥ 5.5 GPa (Fig. 11h) stable immiscibility between a silicate and a carbonate melt disappears and a continuum between carbonatite and silicate melt is now possible.

The available experimental information indicates a broad, suddenly closing immiscibility gap, a narrow pressure and temperature range where carbonate melt forms first and then coexists with silicate melt, and the necessity of a large temperature increase to dissolve silicate components in the carbonate melt at higher pressure. In K₂O + H₂O-free systems, garnet would replace phengite at the left-hand side of the pseudo-binaries, and silicate melting temperatures would lie at values above carbonate melting temperatures. In this case, the topology of Fig. 11d would have a eutectic close to the carbonate composition and would directly continue to the topology of Fig. 11g or Fig. 11h with or without carbonate-silicate melt

immiscibility. It should be noted that at present it is unknown whether carbonate melts would have excess CO₂ with respect to the 1:1 (Ca,Mg,Fe)O:CO₂ ratio in carbonates.

Phengite and clinopyroxene breakdown and their effect on fluid presence and composition

After the breakdown of phengite in the 1:1 wt % H₂O AM composition at $P > 8$ GPa, no hydrous phases could be detected. Phengite is replaced by K-hollandite, which coexists with garnet, cpx, stishovite, kyanite/corundum, ferroan magnesite and aragonite. The absence of any hydrous phase in the AM bulk at > 8 GPa suggests the presence of a H₂O-bearing fluid. In CO₂-free pelites, this fluid would be supercritical with respect to the endpoint of the solidus near 5.5 GPa (Schmidt *et al.*, 2004). Nevertheless, in our H₂O + CO₂ system, this fluid ought to contain both H₂O and CO₂ and, as a carbonate mineral to carbonate melt solidus is clearly defined, the endpoint of the solidus is shifted to higher pressures.

At 16 GPa, after the breakdown of clinopyroxene at *c.* 1300°C, Na is redistributed among the Na-rich Ca-carbonate and, in minor amounts, garnet and K-hollandite. Nevertheless, for both bulk compositions, mass-balance calculations for the cpx-free subsolidus assemblages indicate that 30–50 wt % of the bulk Na₂O is not accounted for by the minerals. Element distribution maps (Fig. 3g) illustrate the presence of small Na-rich pockets ($< 2 \mu\text{m}$) or thin interstitial films in both compositions. The Na-enriched spots in Fig. 3g are neither Ca- nor Si-rich and thus are different from any equilibrium mineral phase. From these observations we interpret the Na-rich regions as quench from a liquid phase and thus deduce the presence of a sodium-rich CO₂ (and H₂O in AM) bearing fluid-like liquid at $P > 16$ GPa at temperatures below the carbonate melting reaction. By analogy to phase relations at crustal pressures, we consider that this Na- and CO₂-rich liquid corresponds to a fluid, whereas the texturally very different carbonate liquid at and above the carbonate-out reaction corresponds to a melt. Further indirect support for the formation of a fluid-like liquid and a transition from fluid-absent to fluid-present conditions with the breakdown of cpx (16 GPa, 1300°C) is the lowering of the solidus temperature by $\geq 50^\circ\text{C}$ in the DG2 bulk. Such a decrease in solidus temperature is not observed for the AM bulk (Fig. 1), which is already fluid-present above 8 GPa. Consequently and unexpectedly, both bulk compositions have the same solidus temperature at > 16 GPa.

The transition from a cpx-bearing to a cpx-free assemblage is a continuous reaction that occurs at different pressures in different bulk compositions. In basaltic compositions cpx decomposes with increasing pressure at

15–17 GPa (at 1400–1800°C; Irifune *et al.*, 1986; Yasuda *et al.*, 1994; Ono & Yasuda, 1996; Okamoto & Maruyama, 2004). In more silica- and alumina-rich compositions (pelites or average continental crust), the transition interval is much wider, and jadeitic cpx can be stable to 24 GPa (Wu *et al.*, 2009). Rapp *et al.* (2008), investigated SiO₂ + Al₂O₃-saturated bulk compositions with variable Na₂O contents and did not find any cpx at 16 GPa, most probably because of the low CaO content and low X^*_{Ca} , the low amount of Na₂O (1.22 wt %) in the bulk with the lowest H₂O content (0.99 wt %), or because of the large quantity of fluid (7.99 wt % H₂O and 2.15 wt % CO₂) in the bulk with higher Na₂O content (4.22 wt %). Wu *et al.* (2009) and Irifune *et al.* (1994) investigated sodium-rich (4.7 and 3.9 wt % Na₂O, respectively) and H₂O-poor (1–2 wt %) compositions with similar CaO contents and X^*_{Ca} to those in this study and found jadeitic cpx stable to 20–24 GPa. In our experiments, we located this transition near 16 GPa, the H₂O-free and more sodium-rich DG2 composition showing a slightly larger cpx stability field. From these considerations, we suggest that the pressure stability of clinopyroxene depends on three major bulk compositional variables: (1) the total Na₂O content of the bulk, with higher Na extending the jadeite stability field; (2) the presence of a fluid dissolving significant amounts of sodium and thus destabilizing jadeitic cpx; (3) alumina saturation, which has an indirect effect on cpx stability, by maintaining the majorite component in garnet at a minimum and the Al content in garnet at a maximum. This leads to a lower Na solubility in our garnets (<1.5 wt % at >16 GPa) compared with garnets from mid-ocean ridge basalt compositions at similar conditions (*c.* 3 wt %; Okamoto & Maruyama, 2004). Thus, alumina saturation tends to stabilize jadeitic cpx and fluid-free, Na-rich, alumina-saturated bulk composition will have cpx stable at the highest pressures (≥ 20 GPa; Irifune *et al.*, 1994; Wu *et al.*, 2009). Fluid- and CO₂-rich alumina-undersaturated systems will allow for partitioning of Na₂O into carbonates, fluid and garnet, potentially leading to the lowest pressure stability of jadeitic clinopyroxene.

The distribution of alkalis in subducted carbonated pelites

At high pressures, the two major alkalis Na and K are normally incorporated in different minerals and show different compatibilities as a function of pressure and temperature. The main minerals that incorporate sodium are (jadeitic) cpx at <16 GPa and Na-rich carbonates at higher pressure. For potassium, the principal phases are phengite in hydrous compositions at <9 GPa, Kfs at $P < 9$ GPa for dry compositions, and K-hollandite for both compositions at higher pressures. K-hollandite also contains some Na, its concentrations increasing with pressure and temperature. In contrast, clinopyroxene dissolves ≤ 1 wt % K₂O, the highest concentrations being observed

at 8 GPa at the lowest temperature (1.03 wt % at 900°C for DG2), near the upper pressure stability of phengite/Kfs. At 6.5 and 8 GPa and temperatures just above the solidus, garnet has K₂O contents of up to 0.6 wt %. The highest potassium contents in garnet are observed at 22 GPa at subsolidus conditions; at this pressure garnet has a surprising 1.15 wt % K₂O, almost the same concentration as for sodium, yielding a total of 2.3 wt % total alkalis. At 22 GPa, the CAS phase also accommodates considerable amounts of alkalis: up to 3.9 wt % K₂O and 0.7 wt % Na₂O at the highest experimental temperature (22 GPa, 1550°C). Considering that all these phases are stable together with K-hollandite at temperatures above the solidus, a significant amount of alkalis could possibly survive the decarbonation process (e.g. during slab stagnation at the 660 km discontinuity).

Naturally occurring potassium phases at high pressures include Kfs, phengite and phlogopite, potassium richterite, phase X, and K-hollandite (for review, see Harlow & Davies, 2004). Nevertheless, potassium may be contained in minor amounts in minerals that are nominally not potassic; for example, cpx with up to 2 wt % K₂O at 7–13 GPa (Tsuruta & Takahashi, 1998; Wang & Takahashi, 1999) and Ca-perovskite with up to 5 wt % K₂O above 20 GPa (Irifune *et al.*, 1994; Okamoto & Maruyama, 2004; Wu *et al.*, 2009). The major Na-rich minerals in peridotitic and basaltic compositions at high pressure are cpx to 17 GPa (Gasparik, 1996) and majoritic garnet at higher pressure, which may accommodate up to 3.0 wt % Na₂O in natural systems (Wang & Takahashi, 1999; Okamoto & Maruyama, 2004; Ghosh *et al.*, 2009) and up to 0.9 Na p.f.u. (*c.* 6–7 wt %) in simplified NMAS systems at 20 GPa (Gasparik, 1996, 2000). Other alumina-rich phases, which substitute for garnet at lower mantle depths, include the CAS, NAL and CF phases, which may also accommodate large quantities of potassium and sodium. This large spectrum of alternative hosts for alkalis at pressures equivalent to the 660 km discontinuity suggests that a large percentage of the alkalis reaching the base of the Transition Zone can effectively be recycled into the lower mantle. In addition, our experiments demonstrate that if melting occurs at depths near the 660 km discontinuity, the residue will acquire an increased K/Na ratio.

The fate of and mass transfer from subducted carbonated pelites

In P – T space, the solidi of the two investigated carbonated pelites (DG2 and AM) are mostly subparallel to typical subduction P – T paths (Fig. 12; Kincaid & Sacks, 1997; van Keken *et al.*, 2002; Peacock, 2003). Nevertheless, in two particular depth ranges carbonated pelites may possibly melt, forming alkali-rich carbonate melts. The first pressure range where decarbonation through melting is plausible in warm subduction zones is between 6 and 9 GPa. In this

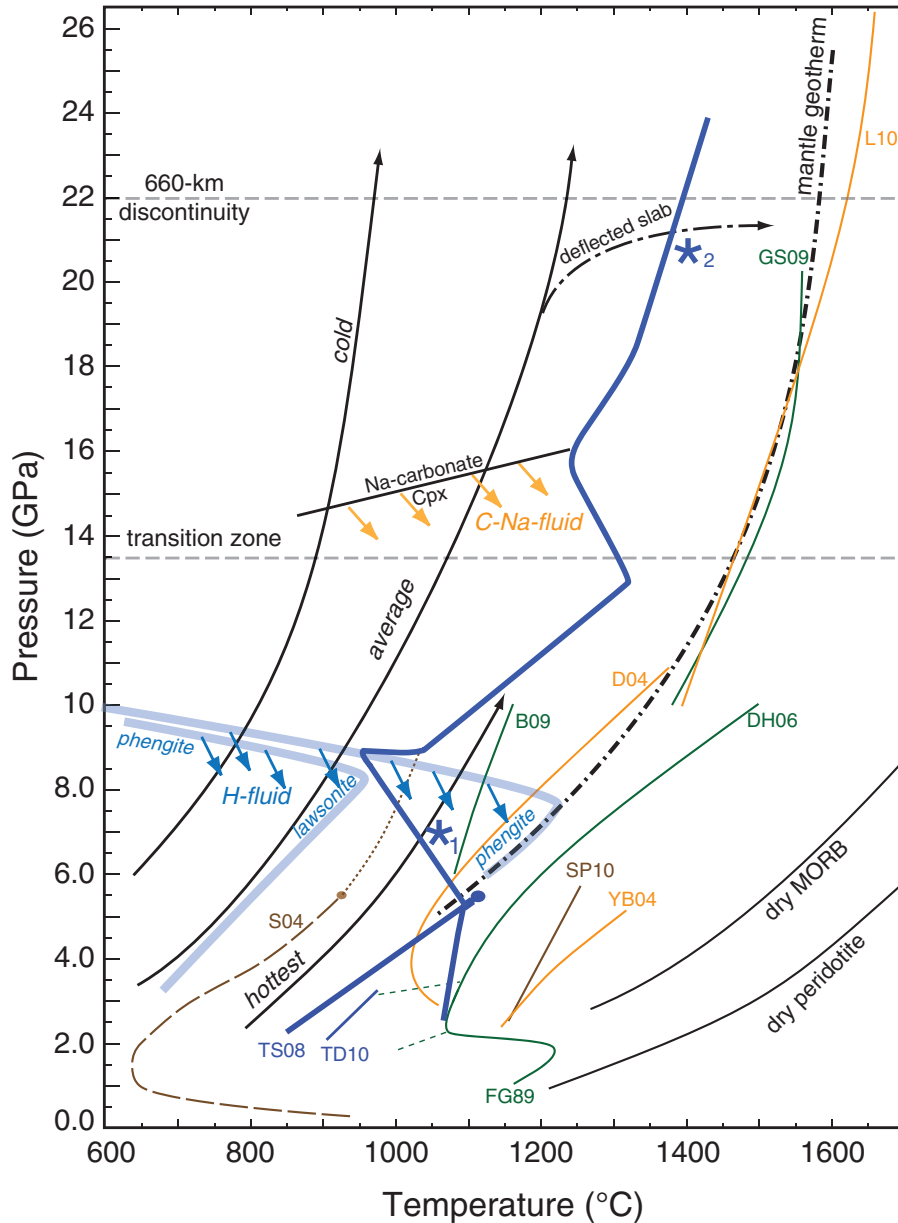


Fig. 12. P - T diagram showing a possible range of subduction P - T paths and the solidi for carbonated pelites, basalts and peridotite. For subducting carbonated pelites or psammites, the solidus corresponds to that of the AM composition up to pressures of phengite-out, at which an H_2O -bearing fluid is liberated and almost all the H_2O is lost from the bulk. At >9 GPa, the carbonated pelite solidus then corresponds to that of the dry DG2 composition. At cpx breakdown, a Na-rich CO_2 fluid is liberated and may cause mantle metasomatism. Typical subduction paths (Kincaid & Sacks, 1997; van Keken *et al.*, 2002; Peacock, 2003) yield melting of these pelites feasible at 6–9 GPa for hot subduction, when P - T paths intersect with the solidus that has a negative Clapeyron slope in this pressure range (blue star labelled 1). If a slab deflects along the 660 km discontinuity, thermal relaxation towards the mantle geotherm (Akaogi *et al.*, 1989) would cause melting (blue star labelled 2). Similarly, at the end of convergence when subduction slows down and thermal relaxation occurs, carbonate melts may form at any depth >5 GPa. Carbonate melts from subducted sediments that rise into the mantle are expected to remain in the liquid state in the mantle as long as oxidizing conditions are maintained. Lines are solidi of subducted material: brown, CO_2 -free pelites; blue, carbonated pelites; orange, carbonated MORB; green, carbonated peridotite. TS08, carbonated pelite (AM composition from 2.5 to 5 GPa) solidus and calcite-out reaction after Thomsen & Schmidt (2008). TD10, solidus for a nominally dry carbonated eclogitic pelite after Tsuno & Dasgupta (2010). D04, YB04, solidi of carbonated basalts after Dasgupta *et al.* (2004) and Yaxley & Brey (2004), the former bulk resulting in dolomite or magnesite, the latter in Mg-calcite. L10, solidus of carbonated basalt simplified in the CaO - MgO - Al_2O_3 - SiO_2 - CO_2 system after Litasov & Ohtani (2011). FG89, Hawaiian Pyrolite + 5 wt % dolomite at ≤ 3.5 GPa (Falloon & Green, 1989). DH06, GS09, solidi of dry carbonated peridotite at high pressure after Dasgupta & Hirschmann (2006) and Ghosh *et al.* (2009). B09, solidus of an H_2O -rich (2.22 wt %) and CO_2 -rich (3.63 wt %) peridotite after Brey *et al.* (2009). S04, melting and dissolution curves for potassium-rich wet sediments after Schmidt *et al.* (2004). SP10, solidus of dry pelite after Spandler *et al.* (2010). The solidus for dry peridotite is after Hirschmann (2000) and that for the dry MORB after Yasuda *et al.* (1994). The stability fields for lawsonite and phengite are after Schmidt & Poli (1998).

pressure range, the carbonated pelite solidus decreases by $>100^{\circ}\text{C}$ and has a negative Clapeyron slope strongly oblique to warm subduction P - T paths. This is particularly true for phengite-bearing assemblages, which are expected during prograde metamorphism of carbonated pelites or psammities. The fact that the pressure interval of 6–9 GPa terminates with the breakdown of two major hydrous phases, phengite and lawsonite (Ono, 1998; Schmidt & Poli, 1998; Okamoto & Maruyama, 2004), and that at 8–9 GPa their devolatilization produces an H_2O -rich liquid, suggests that the solidus of the AM composition (1.1 wt % H_2O) best describes melting at these conditions. Flush melting (Schmidt & Poli, 2004), mediated by a fluid phase produced from lawsonite breakdown in basaltic compositions or from serpentine breakdown in ultramafic rocks, could induce carbonate melting at more moderate temperatures than indicated by our fluid-absent solidus at 8–9 GPa. The melts produced at this depth are carbonate melts with extremely high K/Na ratios (Grassi & Schmidt, 2011).

The second likely melting interval occurs at 20–22 GPa, when the subducting slab reaches the 660 km discontinuity, where it is often deflected (Fukao *et al.*, 2009, and references within). If such slabs remain at constant depth long enough to relax towards adiabatic temperatures, melting would occur in carbonated pelites. Melting at such depths is more probable in cold to average slabs in which the carbonated sediments would not melt between 6 and 9 GPa. The carbonate melts forming at 20–22 GPa are sodium-rich and have $\text{K}_2\text{O}/\text{Na}_2\text{O}$ weight ratios ≤ 0.5 . Gasparik & Litvin (2002) showed that between 20 and 24 GPa, an alkali-rich carbonate melt may coexist with typical mantle assemblages even at 100°C below the mantle geotherm. Based on their experiments and on evidence from inclusions in diamonds (Wang & Sueno, 1996; Wang & Gasparik, 2000), they suggested sodium-rich metasomatism by carbonate melts at the base of the Transition Zone, a scenario for which our study identifies the most likely source.

The two melting scenarios at 6–9 and 20–22 GPa, discussed above, the observation of a mobile Na-rich CO_2 -liquid phase forming at cpx breakdown near 16 GPa, 1300°C , and the fact that our solidi occur at the lowest temperature of any natural carbonated material, render subducted carbonated pelites the prime candidates for supplying metasomatic agents at depth beyond the sub-arc regime. In addition, phengite breakdown, also occurring in CO_2 -free lithologies at 8 GPa, provides an additional source of liquids.

The pressure interval from an eclogite-like cpx-garnet-K-hollandite-stishovite assemblage at ≤ 16 GPa first to a cpx- and then garnet-free perovskite + K-hollandite-bearing assemblage defines the behaviour of the subducted sedimentary material when it reaches the 660 km

discontinuity. In a pyrolitic system, this transition takes place at lower pressures than in a basaltic composition (24–25 and 25–27 GPa, respectively; Irifune & Ringwood, 1993; Litasov & Ohtani, 2005). Our experiments show that this transition in a carbonated pelitic system occurs at even lower pressures for the same temperatures (1400°C). The loss of carbonates through melting at moderate temperatures upon slab deflection at the 660 km discontinuity, combined with the transition to a Ca- and Fe-perovskite-bearing assemblage at lower pressures than in the peridotitic mantle will remove any density barrier for sediments (Irifune & Ringwood, 1993; Irifune *et al.*, 1994; Wu *et al.*, 2009), and promote the subduction of sediments into the lower mantle.

A possible manifestation of Transition Zone carbonated sediment melting

Below eastern Asia, the subducted Pacific slab appears to travel westwards within the mantle Transition Zone just above the 660 km discontinuity (Fukao *et al.*, 2001; Zhao *et al.*, 2004). This observation led to the suggestion that intra-plate volcanoes such as Changbai and Wudalianchi could be regarded as very deep-rooted, back-arc intraplate volcanoes (Zhao *et al.*, 2009). The fast convergence of $7\text{--}10\text{ cm a}^{-1}$ (Taura *et al.*, 2001) should allow for the preservation of carbonates in sediments transported into the Transition Zone. Further westward motion at constant mantle depth causes thermal relaxation and an increase in slab temperature, which may lead to partial melting of carbonated pelites. Low-velocity seismic anomalies in the upper mantle beneath the Changbai and Wudalianchi volcanoes above the subducted Pacific slab (Duan *et al.*, 2009; Zhao *et al.*, 2009) could be associated with ascending magmas generated by melting in the Transition Zone (Duan *et al.*, 2009). Our experiments show that alkalic magnesio- to ferro-dolomitic carbonate melts can be generated from carbonated pelites at these depths, at temperatures far below the mantle adiabat. The addition of small amounts of these volatile-rich, highly-oxidized melts to the Transition Zone mantle would cause a dramatic decrease in the melting temperature of peridotite (Taylor & Green, 1988; Brey *et al.*, 2008), yielding magmas that may ascend to the surface. Contribution of this slab-derived component to the magmas of the Changbaishan volcanic province is consistent with their carbon isotope (Hahn *et al.*, 2008) and trace elements characteristics (Sui *et al.*, 2007).

Carbonatite mantle metasomatism

The presence of small amounts of carbonate melts in the mantle has been proposed to explain several aspects of mantle petrology, chemistry, dynamics and evolution. Under oxidized conditions and in the presence of alkalis, some carbonate melt is expected to be present in a CO_2 -bearing upper mantle at temperatures near, or even

below, a typical mantle adiabat (Dasgupta & Hirschmann, 2007; Brey *et al.*, 2008; Foley *et al.*, 2009; Ghosh *et al.*, 2009). Dasgupta *et al.* (2007) suggested that many alkaline ocean-island basalts (OIB) could be produced by $\sim 1\text{--}5\%$ partial melting of a fertile peridotite source with 0.1–0.25 wt % CO_2 . Presnall *et al.* (2002) pointed out that silicate melting initiated by $\text{CO}_2 + \text{H}_2\text{O}$ may be responsible for a geochemical signature in MORB similar to that attributed to small-degree melts. The presence of carbonate melts or of mantle domains metasomatized by carbonate melts has also been invoked to explain the origin of several highly enriched, ultrapotassic magmas such as kimberlites, orangeites, lamproites, and other alkaline rocks (Girnis *et al.*, 2006; Brey *et al.*, 2008; Dixon *et al.*, 2008).

A carbon-rich mantle, convenient to explain many aspects of the deep Earth, requires an efficient process to return the highly incompatible carbon, transported to the surface with mantle melts, back into the mantle. For this, subduction is the only known process and most of the CO_2 is buried with carbonated sediments and altered oceanic crust (Bonatti *et al.*, 1974; Plank & Langmuir, 1998; Alt & Teagle, 1999). Compared with other carbonated components of the subducting lithosphere (basalts and peridotites), pelites contain much larger concentrations of alkalis and incompatible, lithophile elements. At depths beyond the sub-arc region, carbonated pelites have by far the lowest melting point, which, combined with their position on top of the subducting lithologically stratified oceanic lithosphere, renders them the easiest to melt and consequently the most efficient rock type in the carbon recycling process. Consequently, if melting temperatures were to be reached at depths greater than 170 km (5.5 GPa), carbonated pelites are bound to melt first, generating relatively exotic liquids with an enriched and distinctive chemical signature. Metasomatism by such alkali-rich carbonate melts provides an extremely efficient method to recycle CO_2 , alkalis and many incompatible elements back into the mantle.

Some intra-oceanic magmas have trace element and isotopic compositions suggesting the involvement of enriched components isotopically similar to sediments or upper crustal material in the source region. These components are known as the EM 1 and EM 2 mantle ‘end-members’ (Chauvel *et al.*, 1992; Hofmann, 1997; Eisele *et al.*, 2002). Geochemical modelling suggests that mixing of a depleted mantle component with 5–10 wt % of a sedimentary component can explain the particular trace element enrichment and the radiogenic isotopic composition of the EM mantle types (Chauvel *et al.*, 1992; Eisele *et al.*, 2002).

When comparing the isotopic signature of OIB with their major element composition (Jackson & Dasgupta, 2008; Spandler *et al.*, 2010), potassium enrichment, including $\text{K}_2\text{O}/\text{TiO}_2$ and $\text{K}_2\text{O}/\text{Na}_2\text{O}$ ratios, correlates with $^{87}\text{Sr}/^{86}\text{Sr}$ and $\text{CaO}/\text{Al}_2\text{O}_3$ correlates with $^{206}\text{Pb}/^{204}\text{Pb}$.

Jackson & Dasgupta (2008) suggested enrichment of TiO_2 , K_2O and $\text{K}_2\text{O}/\text{TiO}_2$ in the source of both the EM 1 and EM 2 mantle reservoirs. Assuming that low SiO_2 , high CaO and high $\text{CaO}/\text{Al}_2\text{O}_3$ ratios are related to CO_2 enrichment (Fig. 13a and b), they pointed out that metasomatism via a CO_2 -rich melt or fluid is more likely in EM 2 mantle than in EM 1. The carbonate melts of this study are extremely alkali-rich (potassic to 16 GPa, sodic above) and have high $\text{K}_2\text{O}/\text{TiO}_2$, $\text{CaO}/\text{Al}_2\text{O}_3$ and $\text{K}_2\text{O}/\text{Al}_2\text{O}_3$ ratios and K_2O and TiO_2 contents, in contrast to silicate melts generated from CO_2 -free sediments (Fig. 13). Mixing of sediment-derived carbonate melts with a depleted mantle source (Rehkamper & Hofmann, 1997) results in compositions that fit well with EM 2 OIB rather than EM 1 OIB (Fig. 13d). To fit EM 1 type compositions, a sediment-derived melt with lower Sr concentrations, and thus lower bulk $^{87}\text{Sr}/^{86}\text{Sr}$ after mixing, and/or higher potassium concentrations, is needed. Such a melt is most probably a sediment-derived silicate melt or a supercritical liquid derived from high-pressure high-temperature devolatilization (Kessel *et al.*, 2005).

The low degree of melting in carbonated pelites implies a much higher enrichment of trace elements in this melt relative to the unmelted source. Addition of <2 wt % carbonate melt to the mantle could thus have the same effect as mechanical mixing with 5–10 wt % bulk sediment. Metasomatism via small amounts of alkali-rich carbonate melt is physically easy to achieve and strongly increases the alkali content of the resultant mantle source. Considering all these aspects, we suggest that metasomatism via alkalic dolomitic carbonate melts derived from carbonated pelites is an ideal mechanism to explain the EM 2 mantle reservoir, including its major element characteristics and sedimentary signature.

CONCLUSIONS

- (1) Of all the major subducted rock types, carbonated pelites have the lowest melting point, and are by far the most efficient in recycling CO_2 , alkalis and incompatible elements back into the upper mantle and Transition Zone.
- (2) Comparison of the carbonated pelite solidi with typical subduction P – T paths yields two distinct depth ranges for melting. The first is at 6–9 GPa, where the solidus temperatures of carbonated pelites strongly decrease, most probably as a consequence of the increasingly incompatible behaviour of potassium in this pressure range. The formation of strongly potassic carbonate melts in this depth range could be promoted by flushing with fluids generated from the pressure-induced breakdown of lawsonite, phengite and serpentine in lithologies below the sediment layer. The second is at the base of the Transition

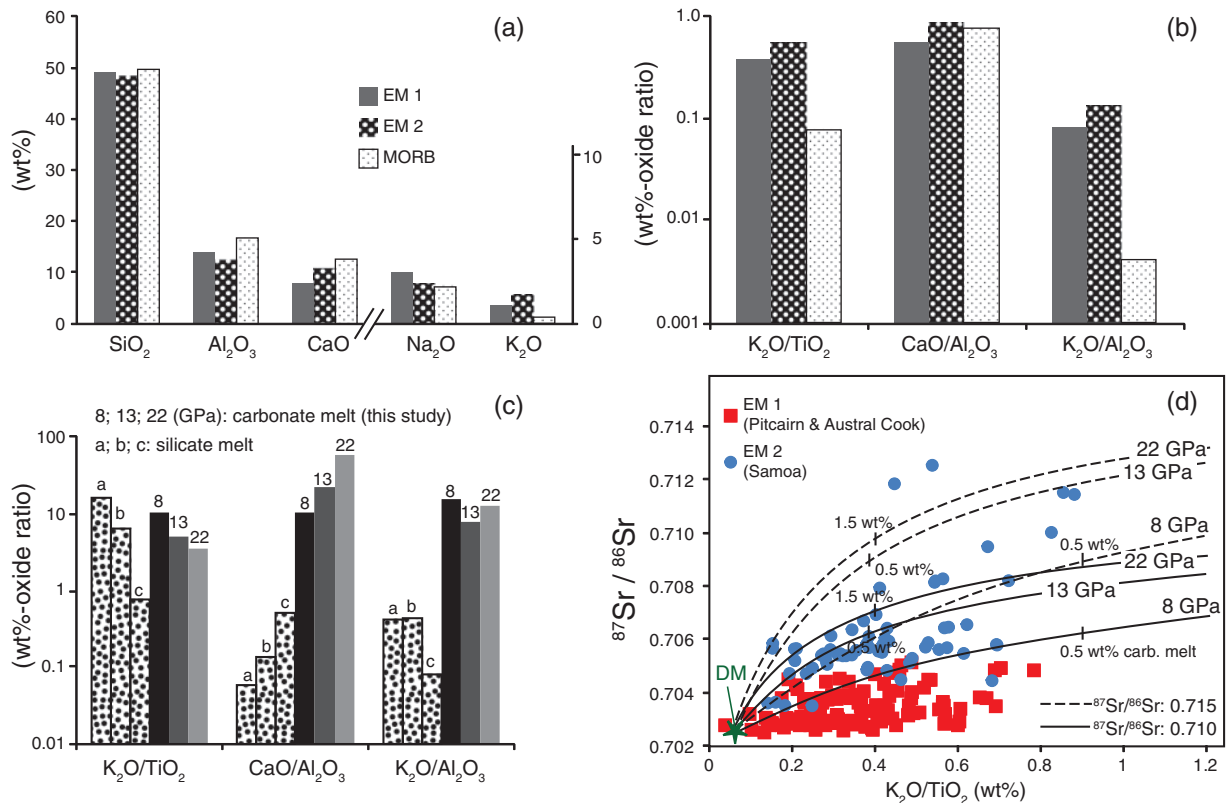


Fig. 13. (a, b) Histograms showing the major element compositional differences in (a) weight per cent and (b) weight ratio between EM 1 and EM 2 type OIB and MORB [data from Jackson & Dasgupta (2008)]. The involvement of carbonate melts is more likely for EM 2 type OIB owing to lower SiO_2 and Al_2O_3 concentrations combined with higher CaO and $\text{CaO}/\text{Al}_2\text{O}_3$ values. (c) Same oxide weight ratios as in (b) for sediment-derived carbonate melts (this study; numbers above columns indicate pressure in GPa) and sediment-derived silicate melts (a, Schmidt *et al.*, 2004 at 5 GPa; b, Spandler *et al.*, 2010 at 5 GPa; c, Irfune *et al.*, 1994 at 20 GPa). (d) $\text{K}_2\text{O}/\text{TiO}_2$ vs $^{87}\text{Sr}/^{86}\text{Sr}$, showing the difference between EM 1 type (red squares) and EM 2 type OIB (blue circles), with EM 2 type having a higher $^{87}\text{Sr}/^{86}\text{Sr}$ for a given $\text{K}_2\text{O}/\text{TiO}_2$ value. Data are from the GEOROC database (<http://georoc.mpch-mainz.gwdg.de/georoc/>). The Sr concentrations (1000–2000 ppm) of the melt used to calculate the mixing lines are from Grassi (2010). Values for the depleted mantle (DM) are from Rehkamper & Hofmann (1997). The isotopic compositions of the sediment-derived melts used in the mixing calculations are 0.710 (continuous lines) and 0.715 (dashed lines), covering a wide spectrum of possible compositions for pelagic sediments mixed with marine carbonates (Rehkamper & Hofmann, 1997; Plank & Langmuir, 1998; Brand *et al.*, 2009).

Zone; melting of carbonated sediments should occur in slabs deflecting along the 660 km discontinuity as a consequence of thermal relaxation towards the mantle geotherm. Melting at such depths would yield highly mobile Na-rich carbonate melts.

- (3) When considering the combination of a low melting point, the position on the top of the slab column and the dynamics of subducting slabs, it is likely that much of the CO_2 trapped in pelitic rocks will be liberated during melting within the upper mantle and Transition Zone. An exception would be the case of cold and fast subducting slabs that might pass directly through the 660 km discontinuity into the lower mantle. Such slabs would recycle carbonated pelites into the lower mantle without melting.
- (4) Metasomatism via alkali-rich dolomitic carbonate melts derived from subducted carbonated sediments

is able to explain some of the features of the EM 2-type mantle reservoir, including its major element characteristics and sedimentary signature.

- (5) The alkali- and Ca-rich, relatively oxidized carbonate melts will be in chemical disequilibrium with the overlying olivine-polymorph-saturated, reduced mantle and thus a large variety of reactions including redox equilibria can be expected upon melt infiltration of the mantle.

ACKNOWLEDGEMENTS

We are grateful to E. Franzolin and U. Mann for discussions improving the paper. Thanks go to D. Mantegazzi for assistance in the Raman spectroscopy, and to A. Rohrbach and C. Liebske for technical support in the laboratory. We are grateful for constructive reviews by

J. Clemens, R. Rapp, and C. Spandler, which all helped to improve this paper.

FUNDING

This study was made possible through grant SNF-200020-120006/1.

SUPPLEMENTARY DATA

Supplementary data for this paper are available at *Journal of Petrology* online.

REFERENCES

- Akaogi, M., Ito, E. & Navrotsky, A. (1989). Olivine-modified spinel–spinel transitions in the system $\text{MgSiO}_4\text{–FeSiO}_4$ —calorimetric measurements, thermochemical calculation, and geophysical application. *Journal of Geophysical Research—Solid Earth and Planets* **94**, 15671–15685.
- Alt, J. C. & Teagle, D. A. H. (1999). The uptake of carbon during alteration of ocean crust. *Geochimica et Cosmochimica Acta* **63**, 1527–1535.
- Blundy, J. & Dalton, J. (2000). Experimental comparison of trace element partitioning between clinopyroxene and melt in carbonate and silicate systems, and implications for mantle metasomatism. *Contributions to Mineralogy and Petrology* **139**, 356–371.
- Blundy, J. D., Falloon, T. J., Wood, B. J. & Dalton, J. A. (1995). Sodium partitioning between clinopyroxene and silicate melts. *Journal of Geophysical Research—Solid Earth* **100**, 15501–15515.
- Bonatti, E., Emiliani, C., Ferrara, G., Honnorez, J. & Rydell, H. (1974). Ultramafic–carbonate breccias from equatorial Mid-Atlantic Ridge. *Marine Geology* **16**, 83–102.
- Brand, U., Tazawa, J., Sano, H., Azmy, K. & Lee, X. Q. (2009). Is mid–late Paleozoic ocean–water chemistry coupled with epeiric seawater isotope records? *Geology* **37**, 823–826.
- Brenan, J. M. & Watson, E. B. (1991). Partitioning of trace-elements between carbonate melt and clinopyroxene and olivine at mantle P – T conditions. *Geochimica et Cosmochimica Acta* **55**, 2203–2214.
- Brey, G. P., Bulatov, V. K., Gurnis, A. V. & Lahaye, Y. (2008). Experimental melting of carbonated peridotite at 610 GPa. *Journal of Petrology* **49**, 797–821.
- Brey, G. P., Bulatov, V. K. & Gurnis, A. V. (2009). Influence of water and fluorine on melting of carbonated peridotite at 6 and 10 GPa. *Lithos* **112**, 249–259.
- Buob, A., Luth, R. W., Schmidt, M. W. & Ulmer, P. (2006). Experiments on $\text{CaCO}_3\text{–MgCO}_3$ solid solutions at high pressures and temperatures. *American Mineralogist* **91**, 435–440.
- Chauvel, C., Hofmann, A. W. & Vidal, P. (1992). HIMU EM—The French–Polynesian connection. *Earth and Planetary Science Letters* **110**, 99–119.
- Connolly, J. A. D. (2005). Computation of phase equilibria by linear programming: A tool for geodynamic modeling and its application to subduction zone decarbonation. *Earth and Planetary Science Letters* **236**, 524–541.
- Dalton, J. A. & Wood, B. J. (1993). The composition of primary carbonate melts and their evolution through wallrock reaction in the mantle. *Earth and Planetary Science Letters* **119**, 511–525.
- Dasgupta, R. & Hirschmann, M. M. (2006). Melting in the Earth's deep upper mantle caused by carbon dioxide. *Nature* **440**, 659–662.
- Dasgupta, R. & Hirschmann, M. M. (2007). Effect of variable carbonate concentration on the solidus of mantle peridotite. *American Mineralogist* **92**, 370–379.
- Dasgupta, R., Hirschmann, M. M. & Withers, A. C. (2004). Deep global cycling of carbon constrained by the solidus of anhydrous, carbonated eclogite under upper mantle conditions. *Earth and Planetary Science Letters* **227**, 73–85.
- Dasgupta, R., Hirschmann, M. M. & Dellas, N. (2005). The effect of bulk composition on the solidus of carbonated eclogite from partial melting experiments at 3 GPa. *Contributions to Mineralogy and Petrology* **149**, 288–305.
- Dasgupta, R., Hirschmann, M. M. & Stalker, K. (2006). Immiscible transition from carbonate-rich to silicate-rich melts in the 3 GPa melting interval of eclogite plus CO_2 and genesis of silica-undersaturated ocean island lavas. *Journal of Petrology* **47**, 647–671.
- Dasgupta, R., Hirschmann, M. M. & Smith, N. D. (2007). Partial melting experiments of peridotite CO_2 at 3 GPa and genesis of alkaline ocean island basalts. *Journal of Petrology* **48**, 2093–2124.
- Dixon, J., Clague, D. A., Cousens, B., Monsalve, M. L. & Uhl, J. (2008). Carbonatite and silicate melt metasomatism of the mantle surrounding the Hawaiian plume: Evidence from volatiles, trace elements, and radiogenic isotopes in rejuvenated-stage lavas from Niihau, Hawaii. *Geochemistry, Geophysics, Geosystems* **9**, doi:10.1029/2008GC002076.
- Duan, Y. H., Zhao, D. P., Zhang, X. K., Xia, S. H., Liu, Z., Wang, F. Y. & Li, L. (2009). Seismic structure and origin of active intraplate volcanoes in Northeast Asia. *Tectonophysics* **470**, 257–266.
- Eisele, J., Sharma, M., Galer, S. J. G., Blichert-Toft, J., Devey, C. W. & Hofmann, A. W. (2002). The role of sediment recycling in EM-1 inferred from Os, Pb, Hf, Nd, Sr isotope and trace element systematics of the Pitcairn hotspot. *Earth and Planetary Science Letters* **196**, 197–212.
- Falloon, T. J. & Green, D. H. (1989). The solidus of carbonated, fertile peridotite. *Earth and Planetary Science Letters* **94**, 364–370.
- Foley, S. F., Yaxley, G. M., Rosenthal, A., Buhre, S., Kiseeva, E. S., Rapp, R. P. & Jacob, D. E. (2009). The composition of near-solidus melts of peridotite in the presence of CO_2 and H_2O between 40 and 60 kbar. *Lithos* **112**, 274–283.
- Fukao, Y., Widiyantoro, S. & Obayashi, M. (2001). Stagnant slabs in the upper and lower mantle transition region. *Reviews of Geophysics* **39**, 291–323.
- Fukao, Y., Obayashi, M. & Nakakuki, T. (2009). Stagnant slab: a review. *Annual Review of Earth and Planetary Sciences* **37**, 19–46.
- Gasparik, T. (1996). Diopside–jadeite join at 16–22 GPa. *Physics and Chemistry of Minerals* **23**, 476–486.
- Gasparik, T. (2000). Evidence for immiscibility in majorite garnet from experiments at 13–15 GPa. *Geochimica et Cosmochimica Acta* **64**, 1641–1650.
- Gasparik, T. & Litvin, Y. A. (2002). Experimental investigation of the effect of metasomatism by carbonic melt on the composition and structure of the deep mantle. *Lithos* **60**, 129–143.
- Gautron, L., Fitz Gerald, J. D., Kesson, S. E., Eggleton, R. A. & Irifune, T. (1997). Hexagonal Ba-ferrite: a good model for the crystal structure of a new high-pressure phase $\text{CaAl}_4\text{Si}_2\text{O}_{11}$? *Physics of the Earth and Planetary Interiors* **102**, 223–229.
- Ghosh, S., Ohtani, E., Litasov, K. D. & Terasaki, H. (2009). Solidus of carbonated peridotite from 10 to 20 GPa and origin of magnesio-carbonatite melt in the Earth's deep mantle. *Chemical Geology* **262**, 17–28.
- Gurnis, A. V., Bulatov, V. K., Lahaye, Y. & Brey, G. P. (2006). Partitioning of trace elements between carbonate–silicate melts

- and mantle minerals: Experiment and petrological consequences. *Petrology* **14**, 492–514.
- Grassi, D. (2010). Melting of subducted carbonated pelites from 5 to 23 GPa: alkali-carbonatites, mantle metasomatism, and element recycling. PhD thesis, ETH Zurich.
- Grassi, D. & Schmidt, M. W. (2011). Melting of carbonated pelites at 8–13 GPa: generating K-rich carbonatites for mantle metasomatism. *Contributions to Mineralogy and Petrology*, doi 10.1007/s00410-010-0589-9.
- Hacker, B. R. (2008). H₂O subduction beyond arcs. *Geochemistry, Geophysics, Geosystems* **9**, doi:10.1029/2007GC001707.
- Hacker, B. R., Abers, G. A. & Peacock, S. M. (2003). Subduction factory—I. Theoretical mineralogy, densities, seismic wave speeds, and H₂O contents. *Journal of Geophysical Research—Solid Earth* **108**(B1), 2029.
- Hahn, D., Hilton, D. R., Cho, M., Wei, H. & Kim, K. R. (2008). Geothermal He and CO₂ variations at Changbaishan intra-plate volcano (NE China) and the nature of the sub-continental lithospheric mantle. *Geophysical Research Letters* **35**, L22304.
- Harlow, G. E. & Davies, R. (2004). Status report on stability of K-rich phases at mantle conditions. *Lithos* **77**, 647–653.
- Hermann, J. & Spandler, C. J. (2008). Sediment melts at sub-arc depths: An experimental study. *Journal of Petrology* **49**, 717–740.
- Hirose, K. & Fei, Y. W. (2002). Subsolvus and melting phase relations of basaltic composition in the uppermost lower mantle. *Geochimica et Cosmochimica Acta* **66**, 2099–2108.
- Hirschmann, M. M. (2000). Mantle solidus: Experimental constraints and the effects of peridotite composition. *Geochemistry Geophysics Geosystems* **1**, 1042–1067.
- Hofmann, A. W. (1997). Mantle geochemistry: The message from oceanic volcanism. *Nature* **385**, 219–229.
- Irifune, T. & Ringwood, A. E. (1993). Phase-transformations in subducted oceanic-crust and buoyancy relationships at depths of 600–800 km in the mantle. *Earth and Planetary Science Letters* **117**, 101–110.
- Irifune, T., Sekine, T., Ringwood, A. E. & Hibberson, W. O. (1986). The eclogite–garnetite transformation at high pressure and some geophysical implications. *Earth and Planetary Science Letters* **77**, 245–256.
- Irifune, T., Ringwood, A. E. & Hibberson, W. O. (1994). Subduction of continental-crust and terrigenous and pelagic sediments—an experimental study. *Earth and Planetary Science Letters* **126**, 351–368.
- Ishibashi, K., Hirose, K., Sata, N. & Ohishi, Y. (2008). Dissociation of CAS phase in the uppermost lower mantle. *Physics and Chemistry of Minerals* **35**, 197–200.
- Jackson, M. G. & Dasgupta, R. (2008). Compositions of HIMU, EMI, and EM2 from global trends between radiogenic isotopes and major elements in ocean island basalts. *Earth and Planetary Science Letters* **276**, 175–186.
- Kerrick, D. M. & Connolly, J. A. D. (2001). Metamorphic devolatilization of subducted marine sediments and the transport of volatiles into the Earth's mantle. *Nature* **411**, 293–296.
- Kessel, R., Ulmer, P., Pettko, T., Schmidt, M. W. & Thompson, A. B. (2005). The water–basalt system at 4 to 6 GPa: Phase relations and second critical endpoint in a K-free eclogite at 700 to 1400°C. *Earth and Planetary Science Letters* **237**, 873–892.
- Kincaid, C. & Sacks, I. S. (1997). Thermal and dynamical evolution of the upper mantle in subduction zones. *Journal of Geophysical Research—Solid Earth* **102**, 12295–12315.
- Leinenweber, K., Linton, J., Navrotsky, A., Fei, Y. & Parise, J. B. (1995). High-pressure perovskites on the join CaTiO₃–FeTiO₃. *Physics and Chemistry of Minerals* **22**, 251–258.
- Litasov, K. D. & Ohtani, E. (2005). Phase relations in hydrous MORB at 18–28 GPa: implications for heterogeneity of the lower mantle. *Physics of the Earth and Planetary Interiors* **150**, 239–263.
- Litasov, K. D. & Ohtani, E. (2009). Solidus and phase relations of carbonated peridotite in the system CaO–Al₂O₃–MgO–SiO₂–Na₂O–CO₂ to the lower mantle depths. *Physics of the Earth and Planetary Interiors* **177**, 46–58.
- Litasov, K. & Ohtani, E. (2011). The solidus of carbonated eclogite in the system CaO–Al₂O₃–MgO–SiO₂–Na₂O–CO₂ to 32 GPa and carbonatite liquid in the deep mantle. *Earth and Planetary Science Letters*, doi:10.1016/j.epsl.2010.03.030.
- Litasov, K. D., Kagi, H., Shatsky, A., Ohtani, E., Lakshtanov, D. L., Bass, J. D. & Ito, E. (2007). High hydrogen solubility in Al-rich stishovite and water transport in the lower mantle. *Earth and Planetary Science Letters* **262**, 620–634.
- Liu, L. G. & El Gorse, A. (2007). High-pressure phase transitions of the feldspars, and further characterization of lingunite. *International Geology Review* **49**, 854–860.
- McCammon, C. A. & Ross, N. L. (2003). Crystal chemistry of ferric iron in (Mg, Fe)(Si,Al)O₃ majorite with implications for the transition zone. *Physics and Chemistry of Minerals* **30**, 206–216.
- Nichols, G. T., Wyllie, P. J. & Stern, C. R. (1994). Subduction zone-melting of pelagic sediments constrained by melting experiments. *Nature* **371**, 785–788.
- Niida, K. & Green, D. H. (1999). Stability and chemical composition of pargasitic amphibole in MORB pyrolyte under upper mantle conditions. *Contributions to Mineralogy and Petrology* **135**, 18–40.
- Okamoto, K. & Maruyama, S. (2004). The eclogite–garnetite transformation in the MORB + H₂O system. *Physics of the Earth and Planetary Interiors* **146**, 283–296.
- Ono, S. (1998). Stability limits of hydrous minerals in sediment and mid-ocean ridge basalt compositions: Implications for water transport in subduction zones. *Journal of Geophysical Research—Solid Earth* **103**, 18253–18267.
- Ono, S. & Yasuda, A. (1996). Compositional change of majoritic garnet in a MORB composition from 7 to 17 GPa and 1400 to 1600°C. *Physics of the Earth and Planetary Interiors* **96**, 171–179.
- Panero, W. R. & Stixrude, L. P. (2004). Hydrogen incorporation in stishovite at high pressure and symmetric hydrogen bonding in delta-AlOOH. *Earth and Planetary Science Letters* **221**, 421–431.
- Panero, W. R., Benedetti, L. R. & Jeanloz, R. (2003). Transport of water into the lower mantle: Role of stishovite. *Journal of Geophysical Research—Solid Earth* **108**(B1), 2039.
- Peacock, S. M. (2003). Thermal structure and metamorphic evolution of subducting slab. In: Eiler, J. (ed.) *Inside the Subduction Factory*. American Geophysical Union, *Geophysical Monograph* **138**, 7–22.
- Philipp, R. W. (1998). Phasenbeziehungen im System MgO–H₂O–CO₂–NaCl. PhD thesis, ETH, Zürich, 185 p.
- Plank, T. & Langmuir, C. H. (1998). The chemical composition of subducting sediment and its consequences for the crust and mantle. *Chemical Geology* **145**, 325–394.
- Presnall, D. C., Gudfinsson, G. H. & Walter, M. J. (2002). Generation of mid-ocean ridge basalts at pressures from 1 to 7 GPa. *Geochimica et Cosmochimica Acta* **66**, 2073–2090.
- Rapp, R. P. & Watson, E. B. (1995). Dehydration melting of metabasalt at 8–32 kbar—implication for continental growth and crust–mantle recycling. *Journal of Petrology* **36**, 891–931.
- Rapp, R. P., Irifune, T., Shimizu, N., Nishiyama, N., Norman, M. D. & Inoue, J. (2008). Subduction recycling of continental sediments and the origin of geochemically enriched reservoirs in the deep mantle. *Earth and Planetary Science Letters* **271**, 14–23.

- Rehkaemper, M. & Hofmann, A. W. (1997). Recycled ocean crust and sediment in Indian Ocean MORB. *Earth and Planetary Science Letters* **147**, 93–106.
- Ryabchikov, I. D., Brey, G., Kogarko, L. N. & Bulatov, V. K. (1989). Partial melting of carbonated peridotite at 50-kbar. *Geochemistry International* **27**(8), 1–6.
- Schmidt, M. W. & Poli, S. (1998). Experimentally based water budgets for dehydrating slabs and consequences for arc magma generation. *Earth and Planetary Science Letters* **163**, 361–379.
- Schmidt, M. W. & Poli, S. (2004). Generation of mobile components during subduction of oceanic crust. In: Rudnick, R. L. (ed.) *Treatise on Geochemistry 3*. Amsterdam: Elsevier, pp. 567–591.
- Schmidt, M. W. & Ulmer, P. (2004). A rocking multianvil: Elimination of chemical segregation in fluid-saturated high-pressure experiments. *Geochimica et Cosmochimica Acta* **68**, 1889–1899.
- Schmidt, M. W., Poli, S., Comodi, P. & Zanazzi, P. F. (1997). High-pressure behavior of kyanite: Decomposition of kyanite into stishovite and corundum. *American Mineralogist* **82**, 460–466.
- Schmidt, M. W., Vielzeuf, D. & Auzanneau, E. (2004). Melting and dissolution of subducting crust at high pressures: the key role of white mica. *Earth and Planetary Science Letters* **228**, 65–84.
- Simons, P. Y. & Dachsille, F. (1967). Structure of TiO_2II , a high-pressure phase of TiO_2 . *Acta Crystallographica* **23**, 334–336.
- Singh, J. & Johannes, W. (1996). Dehydration melting of tonalites. I. Beginning of melting. *Contributions to Mineralogy and Petrology* **125**, 16–25.
- Spandler, C., Yaxley, G., Green, D. H. & Scott, D. (2010). Experimental phase and melting relations of metapelite in the upper mantle: implications for the petrogenesis of intraplate magmas. *Contributions to Mineralogy and Petrology*, doi:10.1007/s00410-010-0494-2.
- Stewart, A. J., van Westrenen, W., Schmidt, M. W. & Melekhova, E. (2006). Effect of gasketing and assembly design: a novel 10/3.5 mm multi-anvil assembly reaching perovskite pressures. *High Pressure Research* **26**, 293–299.
- Sui, J. L., Fan, Q. C., Liu, J. Q. & Guo, Z. F. (2007). Mantle heterogeneity beneath Changbaishan volcanic province: evidence from geochemical study on trace elements and isotopes. *Acta Petrologica Sinica* **23**, 1512–1520.
- Sweeney, R. J., Prozesky, V. & Przybylowicz, W. (1995). Selected trace and minor element partitioning between peridotite minerals and carbonatite melts at 18–46 kbar pressure. *Geochimica et Cosmochimica Acta* **59**, 3671–3683.
- Taura, H., Yurimoto, H., Kato, T. & Sueno, S. (2001). Trace element partitioning between silicate perovskites and ultracalcic melt. *Physics of the Earth and Planetary Interiors* **124**, 25–32.
- Taylor, W. R. & Green, D. H. (1988). Measurement of reduced peridotite–C–O–H solidus and implications for redox melting of the mantle. *Nature* **332**, 349–352.
- Thibault, Y., Edgar, A. D. & Lloyd, F. E. (1992). Experimental investigation of melts from a carbonated phlogopite lherzolite—implications for metasomatism in the continental lithospheric mantle. *American Mineralogist* **77**, 784–794.
- Thomsen, T. B. & Schmidt, M. W. (2008). Melting of carbonated pelites at 2.5–5.0 GPa, silicate–carbonatite liquid immiscibility, and potassium–carbon metasomatism of the mantle. *Earth and Planetary Science Letters* **267**, 17–31.
- Tsuno, K. & Dasgupta, R. (2010). Melting phase relation of anhydrous, carbonated pelitic-eclogite at 2.5–3 GPa and deep cycling of sedimentary carbon. *Contribution to Mineralogy and Petrology*, doi:10.1007/s00410-010-0560-9.
- Tsuruta, K. & Takahashi, E. (1998). Melting study of an alkali basalt JB-1 up to 12.5 GPa: behavior of potassium in the deep mantle. *Physics of the Earth and Planetary Interiors* **107**, 119–130.
- van Keken, P. E., Kiefer, B. & Peacock, S. M. (2002). High-resolution models of subduction zones: Implications for mineral dehydration reactions and the transport of water into the deep mantle. *Geochemistry, Geophysics, Geosystems* **3**(10), 1056.
- Wallace, M. E. & Green, D. H. (1988). An experimental determination of primary carbonatite magma composition. *Nature* **335**, 343–346.
- Wang, W. & Sueno, S. (1996). Discovery of a NaPx –En inclusion in diamond: possible transition zone origin. *Mineralogical Journal* **18**, 9–16.
- Wang, W. Y. & Gasparik, T. (2000). Evidence for a deep-mantle origin of a NaPX –En inclusion in diamond. *International Geology Review* **42**, 1000–1006.
- Wang, W. Y. & Takahashi, E. (1999). Subsolidus and melting experiments of a K-rich basaltic composition to 27 GPa: Implication for the behavior of potassium in the mantle. *American Mineralogist* **84**, 357–361.
- Wu, Y., Fei, Y. W., Jin, Z. M. & Liu, X. Y. (2009). The fate of subducted upper continental crust: an experimental study. *Earth and Planetary Science Letters* **282**, 275–284.
- Yasuda, A., Fujii, T. & Kurita, K. (1994). Melting phase-relations of an anhydrous midocean ridge basalt from 3 to 20 GPa—Implications for the behaviour of subducted oceanic crust in the mantle. *Journal of Geophysical Research—Solid Earth* **99**, 9401–9414.
- Yaxley, G. M. & Brey, G. P. (2004). Phase relations of carbonate-bearing eclogite assemblages from 2.5 to 5.5 GPa: implications for petrogenesis of carbonatites. *Contributions to Mineralogy and Petrology* **146**, 606–619.
- Yaxley, G. M. & Green, D. H. (1996). Experimental reconstruction of sodic dolomitic carbonatite melts from metasomatised lithosphere. *Contribution to Mineralogy and Petrology* **124**, 359–369.
- Yong, W. J., Dachs, E., Withers, A. C. & Essene, E. J. (2006). Heat capacity and phase equilibria of hollandite polymorph of KAlSi_3O_8 . *Physics and Chemistry of Minerals* **33**, 167–177.
- Zhai, S. M. & Ito, E. (2008). Phase relations of $\text{CaAl}_4\text{Si}_2\text{O}_{11}$ at high pressure and high temperature with implications for subducted continental crust into the deep mantle. *Physics of the Earth and Planetary Interiors* **167**, 161–167.
- Zhang, J., Li, B., Utsumi, W. & Liebermann, R. C. (1996). In situ X-ray observations of the coesite stishovite transition: reversed phase boundary and kinetics. *Physics and Chemistry of Minerals* **23**, 1–10.
- Zhao, D. P., Lei, J. S. & Tang, R. Y. (2004). Origin of the Changbai intraplate volcanism in Northeast China: Evidence from seismic tomography. *Chinese Science Bulletin* **49**, 1401–1408.
- Zhao, D. P., Tian, Y., Lei, J. S., Liu, L. C. & Zheng, S. H. (2009). Seismic image and origin of the Changbai intraplate volcano in East Asia: Role of big mantle wedge above the stagnant Pacific slab. *Physics of the Earth and Planetary Interiors* **173**, 197–206.